

5 **Beam Physics Research with the IOTA Electron Lens**

6 **G. Stancari,^{a,1} R. Agustsson,^f N. Banerjee,^c C. Boffo,^a A. Burov,^a K. Carlson,^a B. Cathey,^a**
7 **Y.-C. Chen,^f M. Chung,^h D. Crawford,^a R. Dhuley,^a N. Eddy,^a B. Freemire,^d C. Hall,^g**
8 **Y.-K. Kim,^c A. Kolehmainen,^b V. Lebedev,^a A. Murokh,^f S. Nagaitsev,^{a,c} C. S. Park,^e**
9 **D. Perini,^b A. Romanov,^a J. Ruan,^a V. Shiltsev,^a A. Smirnov,^f E. Stern,^a and A. Valishev^a**

10 ^a*Fermi National Accelerator Laboratory, Batavia, Illinois 60510, USA*

11 ^b*CERN, European Organization for Nuclear Research, CH-1211 Geneva 23, Switzerland*

12 ^c*The University of Chicago, Chicago, Illinois 60637, USA*

13 ^d*Euclid Techlabs, Bolingbrook, Illinois 60440, USA*

14 ^e*Korea University, Sejong 30019, South Korea*

15 ^f*RadiaBeam Technologies, Santa Monica, California 90404, USA*

16 ^g*RadiaSoft, Boulder, Colorado 80301, USA*

17 ^h*Ulsan National Institute of Science and Technology, Ulsan 44919, South Korea*

18 *E-mail: stancari@fnal.gov*

19 **ABSTRACT:** The electron lens in the Fermilab Integrable Optics Test Accelerator (IOTA) will enable
20 new research in nonlinear integrable optics, space-charge compensation, electron cooling, and the
21 stability of intense beams. This research addresses scientific questions on high-brightness beams
22 and operational challenges of high-power accelerators for nuclear and particle physics. We review
23 the roles that electron lenses play in this field and the physical principles behind their applications.
24 The design criteria and specifications for the IOTA storage ring and electron lens are then discussed.
25 We conclude with a description of the components of the apparatus.

26 **KEYWORDS:** Accelerator modelling and simulations, Accelerator subsystems and technologies,
27 Beam dynamics

¹Corresponding author. This manuscript has been authored by Fermi Research Alliance, LLC under Contract No. DE-AC02-07CH11359 with the U.S. Department of Energy, Office of Science, Office of High Energy Physics.

28 **Contents**

29	1 Electron Lenses and the IOTA Research Program	2
30	1.1 The IOTA Storage Ring and Beam Physics Program	2
31	1.2 Roles of the IOTA Electron Lens	4
32	2 Research Areas Based on the IOTA Electron Lens	7
33	2.1 Nonlinear Integrable Optics	7
34	2.1.1 McMillan Lens	7
35	2.1.2 Axially Symmetric Thick Lens	9
36	2.2 Electron Cooling	9
37	2.2.1 Electron Lens as Electron Cooler	9
38	2.2.2 Recombination Rates	11
39	2.3 Tune-Spread Generation for Landau Damping	11
40	2.4 Space-Charge Compensation	12
41	2.4.1 Electron Column	13
42	2.4.2 Space-Charge-Compensating Electron Lens	13
43	2.5 Other Advanced Studies of Beam Dynamics and Stability	14
44	3 Design and Specifications	15
45	3.1 General Layout	15
46	3.2 Storage-Ring Lattice	15
47	3.3 Magnetic System	16
48	3.4 High-Voltage System	17
49	3.5 Electron Beam	17
50	3.6 Vacuum System	18
51	4 Experimental Apparatus	18
52	4.1 Magnetic System	18
53	4.2 Electron Sources	19
54	4.3 Collector	20
55	4.4 Instrumentation and Diagnostics	20
56	4.5 The Fermilab Electron-Lens Test Stand	22
57	5 Conclusions	24

1 Electron Lenses and the IOTA Research Program

In the Fermilab Integrable Optics Test Accelerator (IOTA) [1], a rich beam physics research program has started. Part of this program is based on novel applications of electron lenses. After an introduction on electron lenses and on the IOTA ring, we outline the scientific program, describe the experimental design criteria, and give an overview of the apparatus.

1.1 The IOTA Storage Ring and Beam Physics Program

IOTA is a storage ring dedicated to beam physics research (figure 1). It can operate with both electrons or protons and it is part of the Fermilab Accelerator Science and Technology (FAST) facility [1], which also includes the FAST superconducting linac. The IOTA/FAST complex has three main purposes: (i) to address the challenges posed by future high-intensity machines, such as instabilities and losses; (ii) to carry out basic research in beam physics; and (iii) to provide education and training for scientists and engineers.

IOTA is unique also because of its flexibility. It has a circumference of 40 m and a relatively large aperture diameter (50 mm). It can be reconfigured to accommodate different experiments and, because of the quality of the instrumentation, the magnetic lattice can be precisely controlled. In addition, the lattice itself was designed to have significant flexibility to enable a wide variety of studies. IOTA can store electrons up to a kinetic energy of 150 MeV or protons at 2.5 MeV. The main IOTA parameters are listed in table 1. Because of the relatively fast synchrotron-radiation damping and small equilibrium emittances, electrons are ideal for the study of linear and nonlinear single-particle effects. With protons, on the other hand, very large space-charge tune shifts $\Delta\nu_{sc}$ are achievable. Many fundamental questions on the physics of high-brightness beams can be studied, such as the effect of nonlinear integrable lattices on instability thresholds, the interplay between space charge and nonlinearities, space-charge compensation, emittance evolution, halo formation and beam diagnostics.

One of the pillars of the IOTA research program is the experimental study of nonlinear integrable focusing systems [2–11]. Because of their nonlinearity, these systems generate a betatron tune spread, protecting the beam from instabilities through Landau damping. Integrability ensures that the nonlinearity does not reduce the dynamic aperture of the machine, thus preserving beam lifetime and emittance. The experimental demonstration of these concepts can significantly impact the design and performance of high-intensity accelerators for nuclear and particle physics. Several other topics are being studied in IOTA, such as the statistical properties of undulator radiation [12–14] and the experimental demonstration of optical stochastic cooling [15]. In addition, IOTA has the capability of storing single electrons or a small known number of electrons [16, 17]. Experiments on the coherence properties of two-photon undulator radiation from a single electron, for instance, will take place in the near future.

Electrons were circulated in IOTA for the first time in August 2018. Typically, the machine runs for a few months, after which it is shut down for maintenance and upgrades and reconfigured for the next experimental run. IOTA Run 1 lasted until April 2019. Run 2 took place between November 2019 and March 2020. Currently, the machine is being commissioned for Run 3. Installation of the proton injector is scheduled to be completed at the end of 2021, enabling research on space-charge-dominated beams. The ability to switch between proton and electron operations

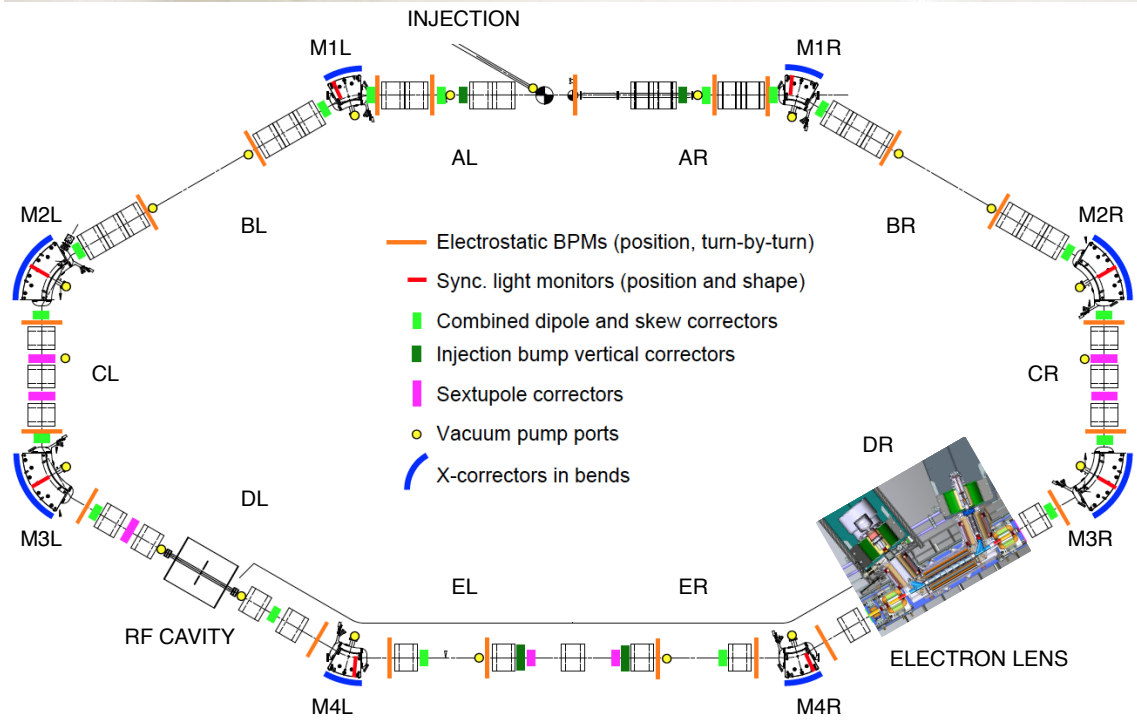
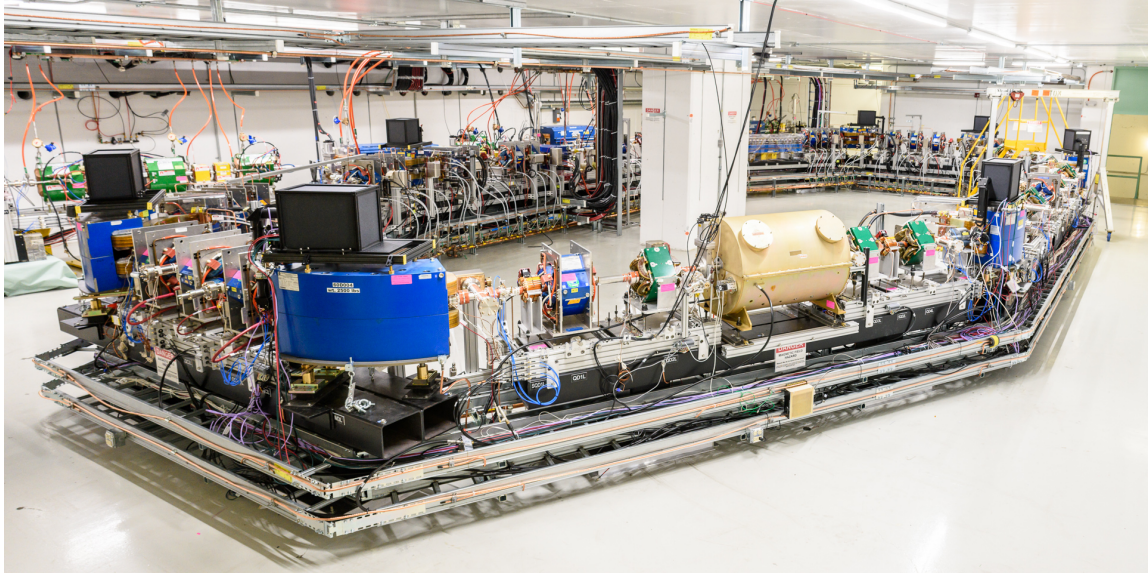


Figure 1. The IOTA storage ring at Fermilab. The layout shows the planned location of the electron lens. The sectors are named AR (A Right), BR, etc. through AL (A Left). The dipole magnets and the corresponding synchrotron-radiation stations are labeled as M1R, M2R, . . . , M1L. (Photo: Giulio Stancari / Fermilab)

99 will be maintained, both for commissioning and for physics. Installation of the IOTA electron
 100 lens is tentatively scheduled for the second half of 2022. More information on the IOTA physics
 101 program can be found on the Web page of the IOTA/FAST Scientific Committee [18].

102 1.2 Roles of the IOTA Electron Lens

103 Electron lenses are a flexible instrument for beam physics research and for accelerator operations.
 104 Several applications were demonstrated experimentally. They were first used in the Fermilab
 105 Tevatron collider for beam-beam compensation, abort-gap cleaning, and halo collimation [19–22].
 106 In the Relativistic Heavy Ion Collider (RHIC) at Brookhaven National Laboratory, electron lenses
 107 allowed experiments to reach significantly higher luminosities [23]. Recently, hollow electron
 108 lenses for active halo control were included among the upgrades of the Large Hadron Collider at
 109 CERN to reach higher luminosities (HL-LHC Project) [24–30]. Future applications also include
 110 space-charge compensation in synchrotrons at FAIR [31].

111 The electron lens is based on low-energy, magnetically confined electron beams overlapping
 112 with the circulating beam in a straight section of a circular particle accelerator or storage ring.
 113 One of the main strengths of electron lenses is the possibility to shape the transverse profile and
 114 time structure of the electron beam to obtain the desired effect on the circulating beam through
 115 electromagnetic interactions [20, 32]. Moreover, the solenoidal magnetic field used in the overlap
 116 region enhances the stability of the two-beam system.

117 Research with electron lenses is an essential part of the IOTA scientific program. First of
 118 all, an electron lens can be used as a nonlinear element to create integrable lattices (section 2.1).
 119 There are at least two ways to accomplish this: (i) the McMillan lens and (ii) the axially symmetric
 120 thick lens. These studies will be carried out with circulating electrons first, then with protons.
 121 Secondly, the electron lens can act as an electron cooler to enable experiments with protons that
 122 require a range of beam lifetimes, emittances and brightnesses (section 2.2). Electron cooling

Table 1. Typical IOTA parameters for operation with electrons or protons.

	Electrons	Protons
Circumference, C	39.96 m	39.96 m
Kinetic energy, K_b	100–150 MeV	2.5 MeV
Revolution period, τ_{rev}	133 ns	1.83 μs
Revolution frequency, f_{rev}	7.50 MHz	0.547 MHz
Rf harmonic number, h	4	4
Rf frequency, f_{rf}	30.0 MHz	2.19 MHz
Max. rf voltage, V_{rf}	1 kV	1 kV
Number of bunches	1	4 or coasting
Bunch population, N_b	$1 e^- - 3.3 \times 10^9 e^-$	$< 5.7 \times 10^9 p$
Beam current, I_b	1.2 pA – 4 mA	< 2 mA
Transverse emittances (rms, geom.), $\epsilon_{x,y}$	20–90 nm	3–4 μm
Momentum spread, $\delta_p = \Delta p/p$	$1-4 \times 10^{-4}$	$1-2 \times 10^{-3}$
Radiation damping times, $\tau_{x,y,z}$	0.2–2 s	—
Max. space-charge tune shift, $ \Delta\nu_{\text{sc}} $	$< 10^{-3}$	0.5

123 has a long history, but this is the first time that cooling and lens capabilities are integrated in a
124 single device. Another important function of electron lenses is their ability to generate tune shifts
125 and tune spreads, tailored to each bunch train, as demonstrated in the Tevatron and at RHIC. For
126 high-energy colliders, electron lenses are the best option to enhance the stabilizing mechanism of
127 Landau damping (section 2.3). In IOTA, we plan to study this option further, with experimental
128 demonstrations of the electron lens as Landau element to suppress instabilities introduced in a
129 controlled way. Finally, the physics and technology of space-charge compensation in rings can
130 be addressed (section 2.4). Demonstrations have been attempted in the past but were never fully
131 achieved. For this purpose, we envisage two scenarios using the IOTA electron lens: (i) an ‘electron
132 column’, where the low-energy electron beam is off, the negative compensating charge is generated
133 by the protons via residual-gas ionization, and the secondary electrons are trapped as a non-neutral
134 plasma column in a Penning-Malmberg configuration; or (ii) an electron lens with transverse and
135 possibly longitudinal profiles tailored to compensate the space charge of the proton beam. These
136 applications are described in more detail in the following sections, together with an outlook on
137 other advanced topics. Part of this research requires circulating electrons for commissioning and
138 to measure linear and nonlinear single-particle effects. Experiments on intensity effects and space
139 charge will be carried out with proton beams.

140 In IOTA, the electron lens will be installed in the DR straight section (figure 1). The length of
141 the section is 1.4 m. The layout of the IOTA electron lens is shown in figure 2. The low-energy
142 electron beam (0.5–10 keV, typically) is generated in the electron gun and transported through

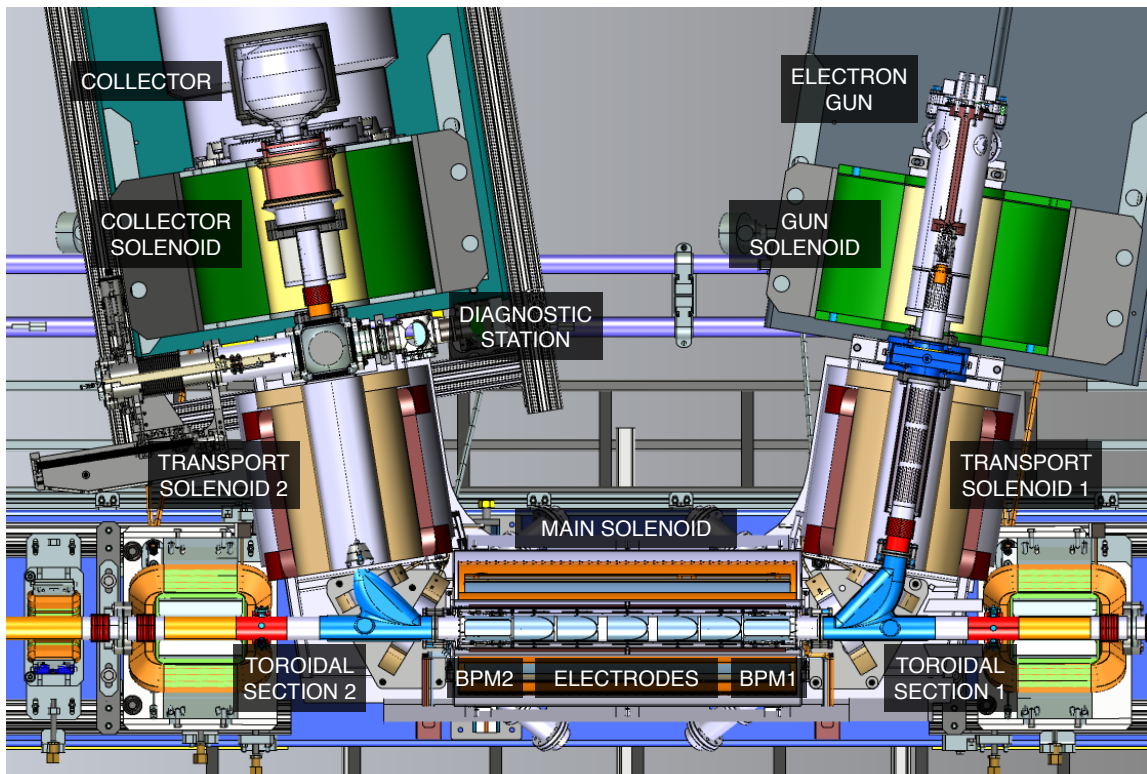


Figure 2. Layout of the IOTA electron lens.

143 solenoid channels and a toroidal section to the overlap region, where it interacts with the IOTA
 144 circulating beam — electrons or protons. It is then directed towards the collector in a similar
 145 way. A summary of the IOTA electron lens parameters is given in table 2. The design criteria are
 146 discussed in more detail in section 3. Some of the main components of the apparatus are described
 147 in section 4.

148 The cathode-anode voltage V determines the velocity $v_e = \beta_e c$ of the electrons in the device,
 149 which has length L and is located in a region of the ring with equal lattice amplitude functions
 150 $\beta_x = \beta_y = \hat{\beta}$. When acting on a circulating beam with magnetic rigidity $(B\rho)$ and velocity
 151 $v_z = \beta_b c$, the linear focusing strength k_e for circulating particles with small betatron oscillation
 152 amplitudes is proportional to the magnitude of the electron current density on axis j_0 :

$$k_e = 2\pi \frac{j_0 L (1 \pm \beta_e \beta_b)}{(B\rho) \beta_e \beta_b c^2} \left(\frac{1}{4\pi\epsilon_0} \right) \frac{q_e q_b}{|q_e q_b|}. \quad (1.1)$$

153 The ‘-’ sign applies when the beams are co-propagating and the electric and magnetic forces act in
 154 opposite directions. The last term contains the charges of the electron beam q_e and of the circulating
 155 particles q_b . It indicates a focusing effect ($k_e < 0$, restoring force) or a defocusing effect ($k_e > 0$).
 156 At large electron beam currents in the electron lens, the focusing of the electron beam itself may of
 157 course distort the lattice. For small focusing strengths and away from the half-integer resonance,
 158 these kicks translate into the tune shift

$$\Delta\nu = -\frac{\hat{\beta} j_0 L (1 \pm \beta_e \beta_b)}{2(B\rho) \beta_e \beta_b c^2} \left(\frac{1}{4\pi\epsilon_0} \right) \frac{q_e q_b}{|q_e q_b|}. \quad (1.2)$$

159 for particles circulating near the axis. Different current-density distributions $j(r)$ introduce a
 160 radial dependence in the focusing strength and therefore different linear or nonlinear effects on the

Table 2. Typical IOTA electron lens parameters.

Parameter	Value
Lattice amplitude functions, $\hat{\beta}$	2–4 m
Circulating beam size (rms), e^-	0.4–0.6 mm
Circulating beam size (rms), p	0.9–4 mm
Circulating beam divergence (rms), e^-	0.15–0.21 mrad
Circulating beam divergence (rms), p	0.3–1.4 mrad
Cathode-anode voltage, V	0.5–10 kV
Peak current, I_e	5 mA – 3 A
Pulse width	200 ns to DC
Pulse repetition rate	DC to 10 kHz
Cathode radius, r_c	< 15 mm
Current-density distributions	McMillan, Gaussian, flat, semi-hollow
Length of the main solenoid, L	0.7 m
Main solenoid field, B_m	0.1–0.5 T
Gun and collector solenoid fields, B_g and B_c	0.1–0.4 T
Beam size compression, $\sqrt{B_m/B_g}$	0.5–2.2
Current-density magnification, B_m/B_g	0.25–5

161 circulating beam. The time structure of the low-energy electron pulse can also be varied, if the
 162 application requires it. This feature can be used, for instance, to adjust focusing strengths for each
 163 bunch or, within limits, for each subset of particles within a bunch.

164 The principle of the electron lens is based on the fact that the electron beam is magnetized.
 165 This means that the electron Larmor radius $r_L = p_\perp/(q_e B)$ is small compared to the transverse
 166 beam size r_b and it is also smaller or of the order of the typical distance between electrons
 167 $r_a = \sqrt[3]{3/(4\pi n_e)}$, to suppress intrabeam scattering. Here p_\perp is the component of the electron
 168 momentum perpendicular to the magnetic field; its distribution depends on the cathode temperature,
 169 emission geometry, and field curvature. The quantity $n_e = j/(q_e v_\parallel)$ represents the electron density.
 170 In a perfectly magnetized beam, the electrons spiral around the field lines. Because current is
 171 conserved, the beam sizes r_g and r_m and current densities j_g and j_m at the gun and main solenoids,
 172 respectively, are related through the ratio of magnetic fields B_g and B_m :

$$B_g r_g^2 = B_m r_m^2, \quad \frac{j_g}{B_g} = \frac{j_m}{B_m}. \quad (1.3)$$

173 In other words, the ratio of the fields is used to control the compression or expansion of the beam.

174 2 Research Areas Based on the IOTA Electron Lens

175 2.1 Nonlinear Integrable Optics

176 A breakthrough in the study of dynamical systems was the realization that nonlinear integrable
 177 optics (NIO) can be implemented in an accelerator with certain lattice symmetries using special
 178 magnets or electron lenses [2–5, 33–36]. The design and first experimental results using nonlinear
 179 magnets in IOTA are described in refs. [6, 8–10]. In the case of electron lenses, two systems have
 180 been identified: (i) the McMillan electron lens and (ii) the axially symmetric thick lens.

181 2.1.1 McMillan Lens

182 In refs. [37, 38], McMillan considered the stability of dynamical systems in general and described
 183 how to build one-dimensional symplectic nonlinear transformations with a conserved quantity,
 184 using geometrical and algebraic arguments. In particular, he showed that if the variables q and p
 185 (representing generic coordinates and momenta, for example) are transformed according to the
 186 nonlinear discrete map

$$\begin{cases} q_{n+1} = p_n \\ p_{n+1} = -q_n + \frac{2\epsilon p_n}{1 + p_n^2} \end{cases}, \quad (2.1)$$

187 the quantity $I_{1D} = q^2 p^2 + q^2 + p^2 - 2\epsilon q p$ is invariant. The value of ϵ parameterizes the strength of
 188 the nonlinearity.

189 The McMillan transformation can be generalized to two dimensions and applied to the trans-
 190 verse motion of a particle in a storage ring [2–4, 33]. The ring is modeled as two main elements: (i) a
 191 linear arc with equal amplitude functions $\beta_x = \beta_y = \hat{\beta}$ at the electron lens and equal phase advances
 192 $\mu_x = \mu_y = 2\pi\nu$ equal to an odd multiple of $\pi/2$, corresponding to a tune $\nu = 1/4$; (ii) a radial nonlin-
 193 ear kick $k_e r/[1 + (r/a)^2]$ at the electron lens, where k_e is the strength (eq. 1.1) and a represents the

194 width of the nonlinear distribution. In Cartesian coordinates ($x, x' = P_x/P_z, y, y' = P_y/P_z$), where
 195 (x, y) is the transverse position and P is the particle momentum (with $P_x \ll P_z$ and $P_y \ll P_z$), the
 196 full one-turn symplectic map has the following form:

$$\begin{cases} x_{n+1} = \hat{\beta}x'_n \\ x'_{n+1} = -\frac{x_n}{\hat{\beta}} + \frac{\hat{\beta}k_e x'_n}{1 + \hat{\beta}^2 \frac{x_n^2 + y_n^2}{a^2}} \\ y_{n+1} = \hat{\beta}y'_n \\ y'_{n+1} = -\frac{y_n}{\hat{\beta}} + \frac{\hat{\beta}k_e y'_n}{1 + \hat{\beta}^2 \frac{x_n^2 + y_n^2}{a^2}} \end{cases}. \quad (2.2)$$

197 This map is integrable, having two independent invariants: the longitudinal component of the
 198 angular momentum

$$L_z = P_z \cdot (xy' - yx') \quad (2.3)$$

199 and the 2D McMillan invariant

$$I = \frac{1}{a^4} \left[\hat{\beta}^2 (x^2 x'^2 + y^2 y'^2) + 2\hat{\beta}^2 x x' y y' + a^2 (x^2 + y^2) + a^2 \hat{\beta}^2 (x'^2 + y'^2) - k_e a^2 \hat{\beta}^2 (x x' + y y') \right]. \quad (2.4)$$

200 The required shape of the nonlinear kicks is generated by the following current-density distri-
 201 bution in the electron lens:

$$j(r) = \frac{j_0}{\left[1 + \left(\frac{r}{a}\right)^2\right]^2}. \quad (2.5)$$

202 The width is parameterized by the value of a , which is also the effective radius for the calculation
 203 of the total current: $I_e = j_0 \cdot (\pi a^2)$, as can be shown by integration.

204 In the linear limit (flat current-density distribution, or $r \ll a$), long-term stability of the iterated
 205 map requires $|\hat{\beta}k_e| < 2$. The tune of particles on axis is then

$$\nu = \frac{1}{2\pi} \arccos\left(\frac{\hat{\beta}k_e}{2}\right) \quad (\text{on axis}) \quad (2.6)$$

206 and it represents the maximum deviation from the unperturbed tune $\nu = 1/4$.

207 Because of the symmetry of the system, it is convenient to use radial and azimuthal coordinates
 208 and momenta

$$\begin{aligned} r &= \sqrt{x^2 + y^2}, & p_r &= \frac{xx' + yy'}{\sqrt{x^2 + y^2}}, \\ \theta &= \arctan2(y, x), & p_\theta &= \frac{xy' - yx'}{\sqrt{x^2 + y^2}}, \end{aligned} \quad (2.7)$$

209 and the conserved component of the angular momentum (divided by the constant longitudinal
 210 momentum):

$$L = L_z/P_z = r p_\theta. \quad (2.8)$$

211 In polar coordinates, the McMillan invariant is

$$I = \frac{\hat{\beta}^2}{a^2} \left(\frac{r^2 p_r^2}{a^2} + \frac{r^2}{\hat{\beta}^2} + p_r^2 + p_\theta^2 - k_e r p_r \right). \quad (2.9)$$

212 The McMillan system can be further generalized to take into account the coupling effect of the
213 electron-lens solenoid.

214 One of the main figures of merit of nonlinear integrable systems in accelerators is the achievable
215 range of betatron tunes or tune spread, on which the stabilization mechanism (Landau damping)
216 is based. In the electron-lens case, small amplitude particles experience the full intensity of the
217 nonlinear kick, whereas particles at large amplitudes are almost unperturbed. For this nonlinear
218 system, it is possible to obtain analytical expressions for the tunes as a function of dimensionless
219 invariants [36]. In ref. [39], the detuning is expressed in terms of the physical parameters $\hat{\beta}$, k_e
220 and a , with additional considerations for experiments in IOTA. For a ‘weak’ nonlinear McMillan
221 lens ($|\hat{\beta}k_e| < 2$), eq. 2.6 yields the maximum detuning. In a strong nonlinear lens ($|\hat{\beta}k_e| \geq 2$), a
222 subset of particles in the beam core experiences the full detuning $\Delta\nu = 0.25$. Therefore, the use of
223 McMillan lenses for nonlinear integrable optics favors lattices with large $\hat{\beta}$ and k_e .

224 2.1.2 Axially Symmetric Thick Lens

225 Another two-dimensional system that can be implemented with electron lenses is one where the
226 axial component of a particle’s angular momentum is conserved together with its Hamiltonian [2].
227 In this case, the nonlinear radial kick can have an arbitrary form. The main requirements are that
228 (i) the kick is given in a region with equal beta functions and (ii) the rest of the ring can be modeled
229 by round linear transformations with phase advances that are integer multiples of π . In a solenoid
230 of length L and axial field B_z , the amplitude function can be kept constant at $\hat{\beta} = 2(B\rho)/B_z$,
231 resulting in a phase advance $\Delta\mu = B_z L/[2(B\rho)] = L/\hat{\beta}$. In this case, the detuning is maximized
232 by increasing the field and length of the solenoid. The effect of the electron lens can be modeled in
233 a symplectic way by interleaving solenoid slices with thin nonlinear kicks.

234 2.2 Electron Cooling

235 One of the key aspects of the IOTA research program is the understanding and control of space-
236 charge-dominated beams. In general, these studies require a range of beam lifetimes and brightnesses
237 and an electron cooler is extremely helpful in providing this flexibility. Moreover, the combination
238 of electron cooling and nonlinear integrable lattices opens up the possibility of exceeding current
239 proton beam brightness limits. Finally, an electron cooler will provide a flow of neutral hydrogen
240 atoms through recombination that can be used for beam diagnostics [40].

241 2.2.1 Electron Lens as Electron Cooler

242 The beam of the IOTA electron lens can be used for cooling protons if their average velocities match
243 ($\beta_e = \beta_b$), corresponding to an electron kinetic energy of 1.36 keV for 2.5 MeV protons.

244 A set of parameters for proton cooling is shown in table 3. The injector can provide a maximum
245 proton current of 8 mA and geometrical rms emittances of about $4 \mu\text{m}$. The parameters are chosen
246 to balance the dominant heating and cooling mechanisms, while achieving significant space-charge
247 tune shifts. At injection, the beam practically fills the transverse and longitudinal apertures. The
248 rms beam sizes correspond to about a quarter of the aperture limits.

249 The main processes leading to emittance growth are intrabeam scattering (IBS) and multiple
250 Coulomb scattering (MCS) on the residual gas. For the parameters in table 3, transverse and

251 longitudinal IBS emittance growth rates are of the order of 10 s. Rates are much faster for particles
 252 at small amplitudes. Adjustments of the cooler settings enable one to control the dependence of
 253 the cooling force on particle amplitude, thus providing a powerful mechanism for manipulating
 254 equilibrium beam distributions. IBS also introduces temperature exchanges between degrees of
 255 freedom, with time scales of about 3 s. Multiple Coulomb scattering gives emittance growth rates
 256 of 20–30 s.

257 Proton losses are caused by single Coulomb scattering (SCS) on the residual gas and by
 258 emittance growth. (Charge neutralization is discussed below.) In IOTA Run 2, with electrons, the
 259 equivalent atomic hydrogen pressure was 5×10^{-8} hPa. At these levels, the SCS maximum lifetime
 260 would be 17 minutes for a zero-emittance beam and considerably shorter for emittances comparable
 261 with the machine acceptance. With protons, vacuum levels need to be in the 10^{-9} hPa range or
 262 better, as electron cooling can counter emittance growth, but it cannot mitigate SCS losses.

263 The maximum electron beam current in the cooler is constrained by the the space-charge voltage
 264 depression $\Delta V \simeq (30 \text{ V/A})I_e/\beta_e$, which causes a corresponding spread in electron velocities. For
 265 cooling, this spread should be of the order of or smaller than the momentum spread of the protons.
 266 For this reason we set $I_e = 10$ mA. The lattice functions are $\beta_x = \beta_y = \hat{\beta} = 4$ m to minimize proton
 267 divergence. The electron beam radius $r_m = 12$ mm is chosen to cover at least 3 standard deviations
 268 of the proton beam size. Under these conditions, cooling times are of the order of 0.1 s and they are
 269 short compared to the IBS and MCS emittance growth rates, as required. The achievable cooling
 270 rates and equilibrium emittances depend on the features of the apparatus, such as the straightness

Table 3. Proton cooling scenario in IOTA.

Proton kinetic energy, K_b	2.5 MeV
Proton velocity parameter, β_b	0.073
Lattice functions at cooler, $\hat{\beta}$	4 m
Transverse machine acceptance, $A_{x,y}$	70 μm
Rf voltage, V_{rf}	0.81 kV
Rf harmonic number, h	4
Relative momentum acceptance, $\hat{\delta}_p$	5.3×10^{-3}
Number of protons per bunch, N_b	3.7×10^9
Proton beam current, I_b	1.3 mA
Transverse emittances (geom., rms), $\epsilon_{x,y}$	4.3 μm , 3.0 μm
Relative momentum spread, δ_p	1.3×10^{-3}
Bunch length, σ_s	0.8 m
Rms beam size at electron lens, $\sigma_{x,y}$	4.1 mm, 3.5 mm
Space-charge tune shift, $\Delta\nu_{\text{sc}}$	-0.5
Electron kinetic energy, K_e	1.36 keV
Electron velocity parameter, β_e	0.073
Electron beam current, I_e	10 mA
Electron current-density distribution	Flat or semi-hollow
Electron beam radius, r_m	12 mm
Electron density, n_e	$5.9 \times 10^{12} \text{ m}^{-3}$

271 of the solenoid field lines, the stability of the high-voltage power supplies, and vacuum. Reductions
 272 of the transverse emittances and momentum spread by about a factor 10 are achievable, with a
 273 corresponding increase in brightness.

274 **2.2.2 Recombination Rates**

275 Radiative recombination $p + e^- \rightarrow H^0 + h\nu$ has proven to be a useful diagnostics for optimizing
 276 cooler settings and to determine the profile of the circulating beam. An overview is given in ref. [41],
 277 whereas ref. [42] describes a recent application. Neutral hydrogen is formed in a distribution of
 278 excited Rydberg states, which have to survive Lorentz stripping through the electron lens toroid
 279 and through the next ring dipole to be detected. For IOTA parameters and magnetic fields, atomic
 280 states up to quantum numbers $n = 12$ can survive. The corresponding recombination coefficient
 281 is $\alpha_r = 9.6 \times 10^{-19} \text{ m}^3/\text{s}$ for a typical electron temperature $k_B T_e = 0.1 \text{ eV}$. The coefficient is
 282 proportional to $1/\sqrt{k_B T_e}$. In the beam frame, transverse electron velocities significantly exceed
 283 those of protons, therefore the recombination rate has a weak dependence on proton velocity. The
 284 total recombination rate R is proportional to the fraction of the ring occupied by the cooler, L/C ,
 285 and to the electron density n_e : $R = N_p \alpha_r n_e (L/C) / \gamma^2$. For the parameters in table 3, one obtains a
 286 rate $R = 1.5 \text{ kHz}$, which is small enough not to significantly affect beam lifetime, but large enough
 287 for cooler tuning and for relatively fast profile measurements (see also section 4.4). As the beam
 288 cools, the size of the electron beam can be reduced, with a corresponding increase in electron
 289 density and recombination rate.

290 **2.3 Tune-Spread Generation for Landau Damping**

291 Suppression of collective instabilities is typically achieved by a combination of feedback systems
 292 and Landau damping [43–45]. For multi-bunch beams, such feedback systems usually suppress
 293 the most unstable coupled-bunch and beam-beam modes. However, having limited bandwidths,
 294 these transverse dampers are normally inefficient for intra-bunch modes, and Landau damping is
 295 needed for their suppression. To make it possible, the spectrum of incoherent (individual particle)
 296 frequencies must overlap with the spectrum of the unstable collective modes, thus enabling the
 297 absorption of the collective energy by the resonant particles. The required frequency spread can
 298 be generated by (i) nonlinear focusing forces, such as those due to the charge distribution of the
 299 opposing beam in colliders, or (ii) by nonlinear magnets, usually octupoles. The first option is not
 300 available for machines with single beams, of course. Even in colliders, the effect is not present at
 301 injection or until the beams are brought into collisions, which themselves generate the required tune
 302 spread through the beam-beam head-on interaction. In octupoles, the transverse magnetic field near
 303 the beam axis is $B_y + iB_x = K_3 \cdot (x + iy)^3$, where K_3 is the strength of the element. The octupolar
 304 field distribution generates betatron frequency shifts proportional to the square of each particle's
 305 oscillation amplitude. As the energy E of the beam increases, the octupoles become less and less
 306 effective: the corresponding frequency spread scales as $1/E^2$, due to both the increased magnetic
 307 rigidity and the smaller beam size, whereas instability growth rates scale only as $1/E$, as the effect
 308 of the transverse beam size is negligible. As a consequence, one needs to increase the strength of
 309 these octupole magnets accordingly. For example, in the Tevatron proton-antiproton collider, with
 310 $E = 1 \text{ TeV}$, there were 35 superconducting octupole magnets installed in 1-m-long cryostats and
 311 operated at currents up to 50 A. In the LHC at 6.5 TeV, 336 superconducting octupole magnets, each

312 about 0.32 m long, operate at the maximum current of 550 A, and even that is not always sufficient
313 to maintain beam stability above certain proton bunch intensities. The anticipated 50 TeV beam
314 energy in the proton-proton Future Circular Collider (FCC-pp) [46, 47] would require a further
315 increase in integrated octupole strength by a factor of more than 60 [48], which makes stabilization
316 with octupoles extremely impractical. Another serious concern is that octupoles, operating at high
317 strengths, induce significant nonlinear fields and frequency shifts for large-amplitude particles, with
318 dangerous destabilizing effects that lead to increased particle losses and radiation loads [49].

319 Electron lenses are ideal for transverse Landau damping, as discussed in ref. [50]. The forces
320 created by a single electron lens can easily introduce the required transverse nonlinear focusing.
321 Unlike a nonlinear magnet, the electron lens generates the tune spread mainly at the beam core, thus
322 mitigating dynamic aperture restrictions and lifetime degradation. (However, see also ref. [51] on
323 the interplay between the number of electron lenses, lattice resonances, and dynamic aperture.)

324 An electron lens in IOTA provides a unique environment to study these effects experimentally.
325 A controlled source of external wake fields (‘antidamper’ or ‘waker’) [52] will be used to induce
326 coherent beam instabilities. A Gaussian electron lens will generate tunable amplitude-dependent
327 frequency spreads. The instability thresholds and growth rates will be measured as a function of
328 electron-lens beam size and current. For instance, calculations showed that the lens is most effective
329 when its transverse rms size does not exceed that of the circulating beam. The possibility to vary
330 the axial magnetic field and the beam emittances is also desirable. Advanced studies of Landau
331 damping with space charge are discussed in section 2.5.

332 2.4 Space-Charge Compensation

333 Novel experimental studies of direct space-charge compensation (SCC) are one of the main research
334 goals of IOTA. Space-charge neutralization and compensation are routinely used in one-pass sys-
335 tems, such as beam lines for low-energy beam transport (LEBT) and rf photoinjectors. In rings, SCC
336 with electrons offers several advantages [32] and could enable higher intensities and brightnesses
337 by reducing losses and emittance growth [51, 53–60]. Proof-of-principle experiments are needed
338 to understand the limits of the method and to explore the stability of the system. For instance, it is
339 not obvious how to mitigate the global effect of charge repulsion with a finite number of localized
340 corrections (such as plasma lenses, beam-beam elements, residual-gas pressure bumps, etc.) over
341 a fraction of the ring circumference. Challenges include the need for high compensating charge
342 densities, the effects of beam-gas interactions, the generation of unwanted lattice distortions, and
343 beam-plasma instabilities.

344 Two concepts of space-charge compensation related to electron lenses were developed:

345 **electron column (*e-column*):** The circulating beam ionizes the residual gas and secondary elec-
346 trons are trapped in a Penning-Malmberg configuration [61, 62] that mirrors as closely as
347 possible the charge density of the beam [63, 64]. No electron gun or collector are used in this
348 case.

349 **space-charge-compensating electron lens (*SCC e-lens*):** The electron gun generates an electron
350 beam with the required intensity and current-density profile, transversely and possibly also
351 in time.

352 2.4.1 Electron Column

353 Early experiments at the Budker Institute for Nuclear Physics in Novosibirsk showed that space-
354 charge limits in a ring could be exceeded by using trapped compensating plasmas [65–69]. Later, the
355 tune shifts induced by trapped electrons could be measured in tests at the Tevatron [70]. However,
356 experiments were limited by vacuum pressures, beam instabilities, poor control of the plasma, or
357 lack of diagnostics. The benefits of using electron columns in the Fermilab Booster were calculated
358 and discussed in refs. [55, 56]. An interesting set of experiments on the interaction of a proton
359 beam with a trapped electron plasma column were conducted at the Indiana University Cyclotron
360 Facility (IUCF) [71, 72].

361 The goals of experiments in IOTA are to characterize the evolution of the non-neutral plasma
362 and to measure the effects on the circulating beam.

363 The electron column is fed by the residual-gas ionization caused by the circulating beam. Cross
364 sections for these processes are collected in ref. [73]. They have typical values of $\sigma_i = 1.7 \times 10^{-21} \text{ m}^2$
365 for protons at 2.5 MeV.

366 The loading time of the column is determined by ionization rate and by the confining forces.
367 The value of the solenoid field B_m should be strong enough to trap electrons radially, while letting
368 ions escape. Longitudinally, electrons are confined with negatively biased electrodes at voltage V_e .
369 This bias voltage also drains ions. Ion recombination and other collisional processes influence the
370 evolution of the electron column as well.

371 Considerable progress has been made in modeling electron columns in IOTA [74–78]. Numerical
372 simulations are challenging because of the very different time scales involved: cyclotron motion,
373 plasma oscillations, and beam revolution period. Also, a large number of particles is necessary to
374 track density fluctuations and halo effects. Assuming a coasting proton beam, the optimization of
375 the confining fields and residual gas pressures using the WARP particle-in-cell code [79, 80] was
376 discussed in ref. [75]. Typical values for IOTA are $B_m = 0.1 \text{ T}$ and $V_e = -5 \text{ V}$. Local residual gas
377 pressures of $p = 5 \times 10^{-4} \text{ hPa}$ are necessary to get a neutralization time $\tau_N \sim 1 \mu\text{s}$, comparable
378 to the proton revolution time $\tau_{\text{rev}} = 1.8 \mu\text{s}$. However, at these pressures, proton lifetime due to
379 single Coulomb scattering and emittance growth is of the order of 0.1 s. This regime may be useful
380 for experimental demonstrations; on the other hand, lower pressures may be sufficient to mitigate
381 slower instabilities. The time structure of the proton beam and the evolution of the column between
382 two beam traversals was studied in refs. [76, 77]. The first model including the full ring with space
383 charge in Synergia [81, 82] was presented in ref. [78]. The next challenge in numerical simulations
384 will be the integration of plasma evolution and ring space charge. Further information on the current
385 status of electron column studies can be found in ref. [83].

386 IOTA provides unique research opportunities for novel studies and systematic measurements
387 of electron columns. One of the most challenging aspects is to accommodate a gas injection system
388 to vary the local residual gas pressure over a wide range, while preserving vacuum levels in the rest
389 of the ring.

390 2.4.2 Space-Charge-Compensating Electron Lens

391 Strong space-charge forces in high-brightness proton beams drive particles to lattice resonances,
392 causing emittance growth, losses and lifetime degradation. Typically, such effects become intoler-

393 able when the space-charge tune-shift parameter $\Delta\nu_{sc}$ reaches the range -0.25 to -0.50 . To reduce
394 these detrimental effects, it was suggested to use electron lenses to compensate the space-charge
395 forces [53]. Further analysis and computer modeling [51, 54, 58–60] indicated that compensation
396 with electron lenses may enable an accelerator to exceed the space-charge limit and to operate with
397 much larger tune-shift parameters, up to -1.0 . The SCC e-lens should have a transverse current-
398 density profile close to that of the proton beam. Interaction of protons with one or more of such
399 devices per turn will result in a reduction of the spread in tunes from $\Delta\nu_{sc}$ to $\Delta\nu_{sc} \cdot (1 - \eta)$, where η
400 is the degree of compensation (in the non-relativistic case). The resulting proton footprint becomes
401 small enough to avoid crossing strong lattice resonances, reducing emittance growth and losses.

402 Experimental SCC studies in IOTA are needed to explore many effects arising in real accel-
403 erators and electron lenses. Both bunched and coasting beams can be used to extend the range
404 of parameters. For instance, the optimal degree of compensation η , predicted to be less than 1,
405 needs to be determined experimentally. Studies showed that the longitudinal profile of the electron
406 current pulse is also critical [51, 57, 59, 60]. One of the challenges lies in the generation of fast
407 electron pulses that match the short bunches in a storage ring. The current state of the art is suffi-
408 cient for the first phase of compensation experiments in IOTA. The full definition of pulse timing
409 requirements for the SCC e-lens is underway. We note that a similar research program, targeted to
410 the synchrotrons for FAIR, is being carried out at GSI [31, 58, 84].

411 2.5 Other Advanced Studies of Beam Dynamics and Stability

412 As a research machine, IOTA is designed to provide a flexible environment for novel investigations
413 under unique experimental conditions. Several advanced research topics related to electron lenses
414 are at the conceptual stage. Here we summarize some of them.

415 The interplay between destabilizing mechanisms, such as space charge and impedances, and
416 mitigation strategies, like cooling, Landau damping, and feedback are of particular scientific interest
417 and technological relevance. For instance, we plan to study the transverse coherent stability limits
418 for bunched beams with strong space charge, beam cooling and nonlinear focusing elements, such
419 as the electron lens. Because machine impedances in IOTA are negligible for proton dynamics, a
420 tunable digital transverse feedback system will be installed to emulate the effects of wakefields [52]
421 (as mentioned in section 2.3).

422 The behavior of coherent instabilities in the presence of strong space-charge forces is of great
423 interest. Studies presented in refs. [85, 86] predicted that there are regimes for which Landau
424 damping with electron lenses, described in section 2.3, is effective under space-charge conditions
425 as well. Experiments with protons in IOTA could shed light on this topic, with a significant impact
426 on the performance of high-intensity accelerators. The IOTA electron lens can also be used for
427 further studies of the head-tail instability due to the skew wake of the magnetized electron beam,
428 predicted in ref. [87].

429 In addition to providing a range of beam parameters for various experiments, the presence of an
430 electron cooler in IOTA enables the investigation of several scientific questions. For instance, when
431 electron cooling is limited by instabilities or by space-charge tune spread, does nonlinear integrable
432 optics combined with cooling enable higher brightnesses? Is it possible to attain record-high stable
433 space-charge tune shifts in the presence of beam cooling by varying the electron beam density
434 distribution and transverse focusing in the rest of the machine? The basic scenario includes an

435 electron lens configured for cooling, as described in section 2.2. Integrability and tune spreads are
 436 provided separately by nonlinear magnets. An appealing but more challenging solution would be
 437 to combine in the same device (the electron lens) both cooling and nonlinear focusing, although
 438 preliminary studies indicate that it is difficult to combine both the constraints of cooling and the high
 439 currents needed to achieve sizable tune spreads. A related topic, the use of a McMillan electron
 440 lens to mitigate space charge, is discussed in refs. [88, 89]

441 3 Design and Specifications

442 The research program based on the IOTA electron lens is wide and exciting. The main challenge
 443 is to incorporate several functions in a single compact device. Beam physics goals and operational
 444 considerations dictate the functional requirements. A summary of the main parameters is presented
 445 in table 2. Here we discuss some of the design considerations.

446 3.1 General Layout

447 The electron-lens assembly must fit in one of the IOTA straight sections (DR in figure 1). The
 448 maximum available axial length is 1.4 m. Displacing the quadrupoles on each end to increase this
 449 length would affect the symmetry of the ring and the minimum achievable amplitude function $\hat{\beta}$.
 450 Taking into account the space needed for the toroidal section and dipole correctors, this leaves about
 451 0.7 m for the main solenoid.

452 The low-energy electron beam co-propagates with the circulating beam to make electron
 453 cooling possible. This choice has a small effect on the maximum achievable kicks (eq. 1.1).

454 3.2 Storage-Ring Lattice

455 For nonlinear integrable optics, the ring lattice must provide the required phase advances and
 456 amplitude functions. The ring was designed to control phase advances at the level of 10^{-3} and beta
 457 functions within 1%. Experiments on single-particle dynamics will be conducted with a pencil beam
 458 of electrons, observing tunes and intensities as a function of kicker amplitude with turn-by-turn
 459 (TBT) beam position monitors (BPMs). For the McMillan lens, the amplitude function $\hat{\beta}$ should
 460 be as large as possible, whereas the axially symmetric thick-lens configuration requires a large
 461 solenoidal field and, therefore, a small beta function. The IOTA focusing lattice was designed to
 462 provide equal amplitude functions around the region of the electron lens in the range $2 \text{ m} \leq \hat{\beta} \leq 4 \text{ m}$
 463 and with vanishing slope (Courant-Snyder parameters $\alpha_{x,y} = 0$). The corresponding values of the
 464 main solenoid field $B_m = 2(B\rho)/\hat{\beta}$ are reported in table 4. For lattice and momentum flexibility,
 465 we require that the main solenoid provide at least $B_m = 0.7 \text{ T}$ in operations, with a maximum of
 466 0.8 T for the engineering design as a safety margin [90]. For electron cooling, it is preferable to use
 467 the larger beta function values and minimize beam divergence. This range of beta functions is also
 468 appropriate for space-charge compensation, where electron lens and circulating proton beam sizes
 469 should be matched.

470 The IOTA lattices for NIO experiments are shown in figure 3. The coupled lattice func-
 471 tions $\beta_x \equiv \beta_1$ (black) and $\beta_y \equiv \beta_2$ (red, both on the left vertical scale) (Edwards-Teng parameteri-
 472 zation [91–93], calculated with MAD-X [94]) and the horizontal dispersion D_x (green, on the right
 473 vertical scale) are plotted as a function of the distance s along the ring, starting from the injection

474 point (see also figure 1). The location of the electron lens is highlighted in orange. The left plot
 475 refers to the McMillan lens case, with $\hat{\beta} = 4$ m, whereas the right plot is for the axially symmetric
 476 thick lens, where $\hat{\beta} = 2$ m.

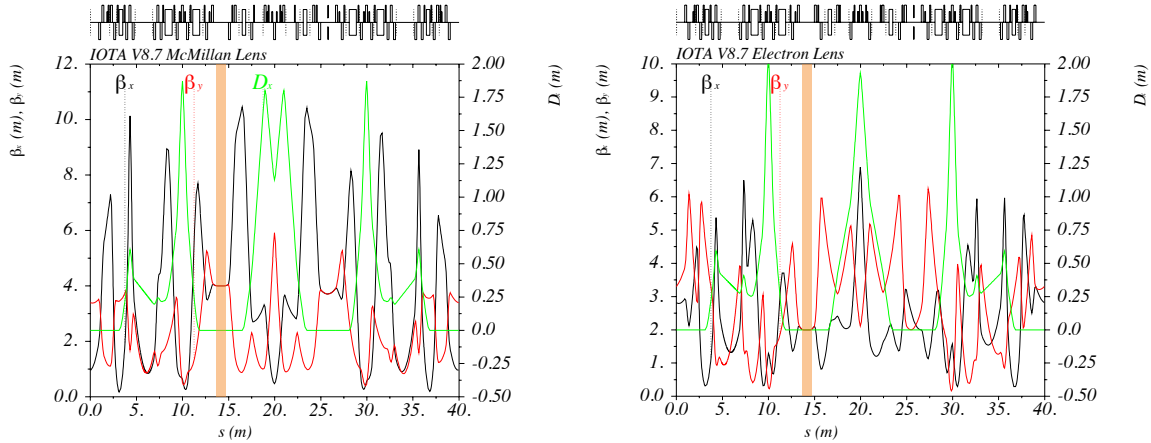


Figure 3. IOTA lattices for electron lens experiments.

477 3.3 Magnetic System

478 The magnetic system has several functions. First of all, it should transport the beam from the
 479 electron gun to the overlap region and, finally, to the collector with an efficiency $> 99\%$ for beam
 480 radii < 15 mm and for all magnetic field configurations. The electron beam should be magnetized,
 481 i.e. with a Larmor radius much smaller than the typical beam sizes and smaller than the average
 482 separation between individual electrons, as discussed in section 1. Secondly, the ratio of the gun
 483 and main solenoid fields B_g/B_m determines the compression and therefore the beam size and
 484 affects the temperature of the beam in the overlap region. Moreover, the field stabilizes $e-p$ beam
 485 oscillations [87, 95, 96].

486 The bore of the main solenoid must be large enough to accommodate the beam pipe, flanges,
 487 and feedthroughs for instrumentation. In the current design, the bore diameter is 115 mm. The main
 488 solenoid should be as long as possible, with a minimum length of 0.7 m. The minimum magnetic
 489 field seen by the low-energy electron beam should be as large as possible and at least 0.1 T. The
 490 distance between the axis of the main solenoid and the trajectory of the low-energy beam with
 491 correctors off should be within 1 mm. For alignment with the circulating beam, the trajectory of the
 492 low-energy beam in the main solenoid should be adjustable in both horizontal and vertical positions
 493 and angles. The position adjustments should have a range of ± 10 mm with 0.03 mm resolution.

Table 4. Lattice requirements on main solenoid field.

Species	Kinetic Energy [MeV]	Magnetic Rigidity [T m]	Main Solenoid Field [T]	
			$\hat{\beta} = 2$ m	$\hat{\beta} = 4$ m
Electrons	150	0.50	0.50	0.25
Protons	2.5	0.23	0.23	0.11

494 Angles should be adjustable in the range ± 5 mrad with resolution $50 \mu\text{rad}$. Field distortions in the
495 good field region of the main solenoid should be $(B_{\perp}/B_z) < 2 \times 10^{-4}$. This requirement is mainly
496 dictated by electron cooling. The good field region of the main solenoid should be at least 0.6 m
497 long and have a transverse diameter of at least 30 mm, corresponding to more than half of the IOTA
498 aperture.

499 3.4 High-Voltage System

500 We plan to use electron beams up to 10 keV. Several electron guns we designed and built have been
501 operated at these voltages without breakdowns. Moreover, at these energies, emission of X-rays is
502 negligible.

503 For beam extraction, in addition to using the electron gun in direct-current (DC) mode, we
504 plan to pulse the cathode-anode voltage with a high-voltage modulator. State-of-art devices with
505 rise times (10%–90%) of less than 100 ns, repetition rates up to 50 kHz, and pulse widths as short
506 as 200 ns are adequate for most applications identified so far. Electron guns have anode-cathode
507 capacitances of the order of 50 pF, which, together with the associated electronics, limit the rise time
508 and repetition rate of the electron pulses. Gating electron-gun emission with grids is possible, but
509 it may cause losses and profile distortions. Matching the longitudinal distribution of the circulating
510 bunches (a few nanoseconds for electrons and a few tens of nanoseconds for protons) requires
511 further developments in electron-gun and modulator technology.

512 The high-voltage circuit includes separate bias voltages for the cathode, the electrodes and
513 the collector. With this arrangement, the beam is decelerated before depositing its energy on the
514 collector. In addition, the functions of high-current supply and precision beam energy setting are
515 separated.

516 3.5 Electron Beam

517 The properties of the electron beam are of course key in an electron lens. For nonlinear integrable
518 optics, the current-density distribution should be sufficient to generate large tune spreads within the
519 machine aperture. To exploit the full detuning $\Delta\nu = 0.25$ in the McMillan case, we need $|k_e| \geq 2/\hat{\beta}$.
520 A high current requirement comes from a scenario with 150 MeV circulating electrons, $\hat{\beta} = 4$ m
521 and $k_e = 0.5 \text{ m}^{-1}$, resulting in $j_m \geq 10 \text{ A/cm}^2$ for a typical electron-lens energy of 6 keV. The
522 size of the low-energy beam should be larger than the size of the pencil beam and at the same time
523 small enough so that the full detuning can be achieved within the available good-field aperture of
524 the machine (about 12 mm in radius). For the McMillan lens, we choose the parameter a (eq. 2.5)
525 in the main solenoid $a_m = 2$ mm. The required beam current is therefore $I_e = j_m \cdot (\pi a_m^2) = 1.3$ A at
526 6 kV, which can be achieved in an electron gun with perveance $P = 2.8 \mu\text{A/V}^{3/2}$. Other scenarios
527 and applications require less current.

528 The ability of generating and transporting different transverse current-density profiles is one of
529 the strengths of electron lenses. This is usually done by replacing the electron gun, although some
530 limited flexibility can be achieved by controlling electrode potentials within the same source. For
531 nonlinear integrable optics, we require a McMillan profile (eq. 2.5), which is a new development.
532 Tolerance studies on the required accuracy are underway. McMillan or Gaussian profiles are
533 adequate for NIO experiments with axially symmetric thick lenses. For electron cooling, a flat or

534 partially hollow profile is used. For the SCC e-lens and for tune-spread generation, a Gaussian
535 distribution can be employed in the first round of experiments.

536 Preservation of the profile from the source to the overlap region relies on the strength and
537 quality of the magnetic fields. Distortions of the beam trajectory and of the current-density profile
538 arise mainly from field curvature (in the toroidal section, for instance) and from self fields. They
539 must be evaluated and mitigated, usually by reducing imperfections and by increasing the minimum
540 axial field seen by the beam. Because of the $B \times \nabla B$ force, the toroidal sections introduce a shift
541 in the trajectory of the centers of gyration perpendicular to the plane of the lens, which must be
542 kept within about 2 mm. As regards the current-density profiles, experimentally one observes
543 that they scale with electron beam current and confining axial field according to the expected
544 space-charge evolution [97, 98]. In particular, similar profiles are obtained for a given family
545 of experimental conditions with constant ratio \sqrt{V}/B , where B represents the effective average
546 value of the axial fields, assumed to scale proportionally ($B \propto B_m \propto B_g$). This ratio is related
547 to the space-charge evolution number $g = \omega_D \cdot \tau_e \propto \sqrt{V}/B$, representing the number of $E \times B$
548 rotations in the propagation time τ_e , with $\omega_D \equiv \omega_{pe}^2/(2\omega_{ce})$ the diocotron (slipping-stream)
549 angular frequency, $\omega_{pe} = \sqrt{q_e^2 n_e / (\epsilon_0 m_e)}$ the plasma angular frequency, and $\omega_{ce} = q_e B / (\gamma_{\perp} m_e)$
550 the cyclotron frequency of the magnetically confined electrons [99]. Beyond analytical estimates,
551 numerical simulations are necessary to evaluate the effects of distortions on profiles. A study was
552 described in ref. [100], using the BENDER particle-in-cell code [101]. Other efforts based on the
553 WARP code [79, 80] and on the commercial software COMSOL [102] and CST STUDIO SUITE [103]
554 are ongoing. In the end, the requirements on electron beam profiles translate into an interplay
555 between source geometry, accelerating voltages, and magnetic field configurations.

556 3.6 Vacuum System

557 The vacuum system must maintain pressures below 10^{-6} hPa in the region of the heated cathode.
558 The assembly is designed so that electron guns can be valved out, swapped and pumped down in
559 a few hours. In the overlap region, residual-gas pressures seen by the circulating beam should be
560 less than 10^{-9} hPa for electrons and 10^{-10} hPa for protons. Controlled gas injection for e-column
561 applications and, possibly, for ionization profile monitors (section 4.4) presents a challenge and
562 solutions are under study.

563 4 Experimental Apparatus

564 The general layout of the IOTA electron lens is shown in figure 2. Here we discuss some of the
565 features of the subsystems.

566 4.1 Magnetic System

567 The current configuration of the magnetic system includes the following components:

- 568 • 1 gun and 1 collector solenoid, with 4 corrector coils each.
- 569 • 2 transport solenoids, with 4 corrector coils each.
- 570 • 2 short solenoids in each of the 2 toroidal sections.

- 571 • 1 main solenoid with 8 corrector coils: 4 short ones upstream for horizontal and vertical position
572 adjustments and 4 long ones downstream for horizontal and vertical angle adjustments.
- 573 • 2 orbit correctors (not shown in figure 2) for the circulating beam to compensate for the
574 transverse kicks due to the toroidal sections, 1 just upstream and 1 downstream of the electron
575 lens.

576 The gun and collector solenoids are available. They were recovered from one of the Tevatron
577 electron lenses (TEL-2) [20]. The transport solenoids, the toroidal sections and the orbit correctors
578 need to be built. For the main solenoid, we are considering a conduction-cooled, cryogen-free
579 superconducting solenoid. A view is shown in figure 4. This choice implies compact coils,
580 improved field quality, and lower power consumption compared to a resistive solenoid. These
581 systems are reliable and well supported and cool-down times are compatible with IOTA operations.
582 The design of the coils and quench protection system is underway. The current status of the design
583 is described in detail in refs. [90, 104].

584 4.2 Electron Sources

585 Several electron guns were built at Fermilab over the course of the years for the Tevatron electron
586 lenses, as prototypes for the LHC, and for general research and technological developments. They
587 are based on thermionic emission from porous tungsten dispenser cathodes with $\text{BaO}:\text{CaO}:\text{Al}_2\text{O}_3$
588 impregnant, operating at temperatures around 1200 K. These designs are robust and reproducible
589 and routinely yield current densities of the order of 4 A/cm^2 . New technological developments
590 have made designs based on scandate cathodes viable for aerospace applications and accelerators.
591 In collaboration with CERN [26, 105], they are being considered in cases where larger current
592 densities or lower operating temperatures are required. Although we have not been able to pursue it
593 so far, another development that would significantly simplify the design of compact electron lenses
594 are axially symmetric sources and collectors mounted around the main beam pipe, eliminating the
595 need for the toroidal sections [106–108].

596 Figure 5 shows a photograph of the 10-mm-diameter electron gun used in the Tevatron for beam-
597 beam compensation studies. Measurements of the current-density profile taken at the Fermilab

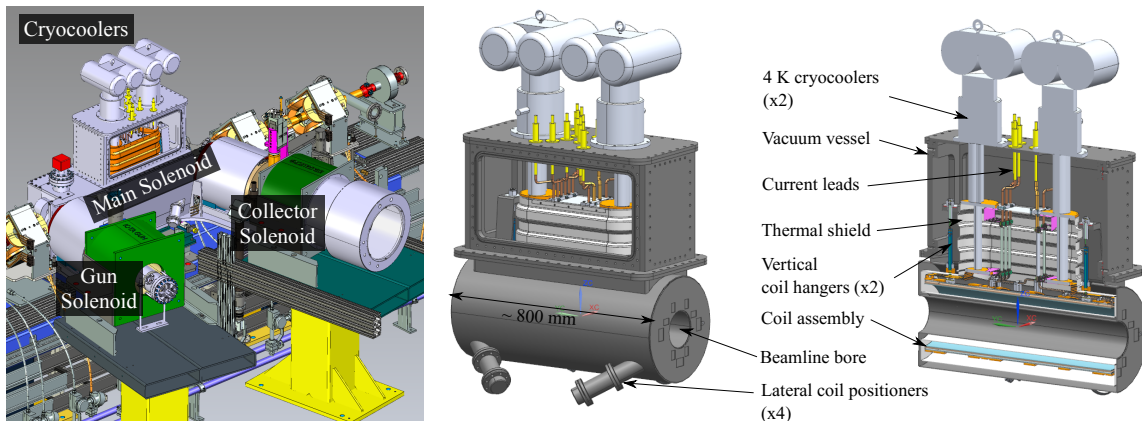


Figure 4. Layout of the superconducting option for the main solenoid.

598 electron-lens test stand (see section 4.5) are also shown. This electron source can be reused in
599 IOTA for NIO studies, in the SCC e-lens configuration, or for the generation of tune spreads. New
600 cathodes are available if replacements are needed.

601 For the IOTA research program, it is important to maintain and develop the capability to design
602 and build new electron sources, such as the McMillan electron gun for NIO or flat and semi-hollow
603 guns for electron cooling.

604 4.3 Collector

605 The collector is reused from one of the Tevatron electron lenses (TEL-2) [20]. It is made of copper
606 with a ceramic gap insulating it from the vacuum chamber. The assembly is water cooled and has a
607 power rating of 50 kW, well exceeding the maximum beam power anticipated for the IOTA electron
608 lens.

609 4.4 Instrumentation and Diagnostics

610 Beam diagnostics is critical for a research machine like IOTA. Here we mention instrumentation
611 that is directly related to the electron lens, as well as other diagnostic devices that are relevant for
612 the research program.

613 The current and pulse structure of the low-energy electron beam is measured with 2 passive
614 beam current transformers, one at the cathode and one at the collector.

615 A diagnostic station was designed to provide profile measurements of the magnetized beam
616 (figure 6). The station is located just upstream of the collector, to minimize its influence on beam
617 dynamics in the overlap region. If necessary, another station could be installed just downstream
618 of the electron gun to measure beam properties at the source. At low electron beam currents
619 ($\lesssim 100$ mA peak), fast profile imaging is provided by a retractable YAG screen and a CCD camera.
620 At higher intensities, a TZM-alloy plate with a pinhole and Faraday cup can be scanned across the
621 beam to measure current density as a function of transverse position. Most components have been
622 procured. The stations need to be assembled and tested. A similar setup is used for the RHIC
623 electron lenses, as described in refs. [109, 110].

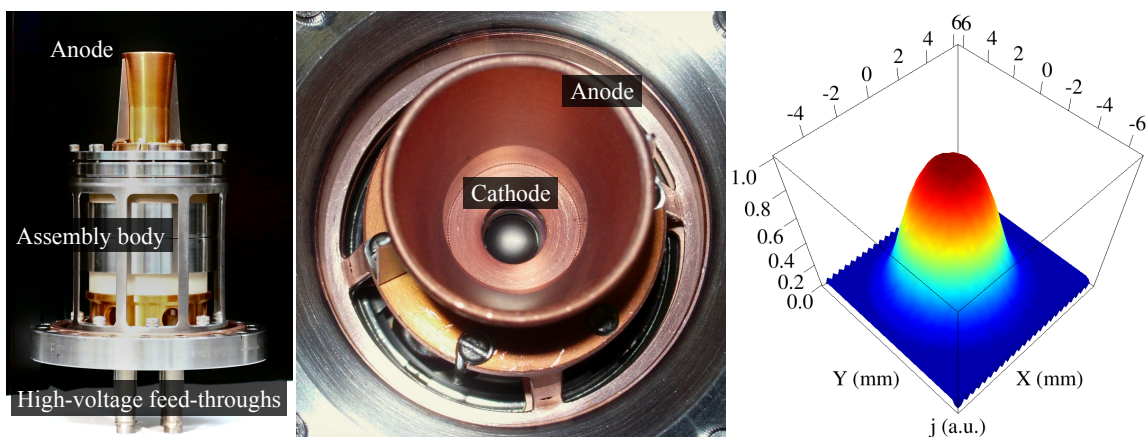


Figure 5. Gaussian electron gun.

624 In addition to the 21 button BPMs in the ring, 2 BPMs are included in the beam pipe inside the
625 main solenoid for aligning the low-energy electron beam with the circulating beam. The current
626 design includes strip-line pickups to enhance the signal and to accommodate the different time
627 structures of electron-lens pulses, 150 MeV electrons and 2.5 MeV circulating protons. However,
628 preliminary estimates indicated that button BPMs may also be adequate.

629 A set of 5 biased diagonally-split cylindrical electrodes is foreseen for the central section
630 of the electron lens to cover several functions. The electrodes can be used as transverse and
631 longitudinal pickups for additional beam position monitoring, pulse timing and, in the case of
632 the e-column, to detect plasma oscillations. When biased, they will be used for clearing trapped
633 ions in the circulating electron beam or to confine the electron column during proton operations.
634 The measured bias current is an indication of electron or ion fluxes. One of the electrodes, with
635 8 sectors, may be employed to implement the ‘rotating-wall’ technique to study the stabilization of
636 the electron column [62, 111, 112].

637 Advanced instrumentation to measure beam intensities, emittances and losses over the time
638 scales of instability growth is essential to characterize the dynamics of high-brightness space-
639 charge-dominated proton beams. Various options are being considered for continuous monitoring
640 of proton transverse profiles and emittances. The first option is a compact gas-sheet profile monitor
641 (GSPM), which was built and characterized [9, 113]. In the GSPM, a compressed gas (N_2) is
642 forced through a nozzle. As the gas travels downstream, it exhibits molecular flow due to the high
643 Knudsen number. The gas then reaches a skimmer, which removes any molecules with significant
644 divergence and provides the final shape. The resulting sheet is then injected at an angle transversely
645 to the direction of the proton beam. The beam ionizes the gas and the ions are extracted by a series
646 of annular electrodes. Microchannel plates (MCPs) convert the ions to electrons and yield a typical
647 amplification factor of 10^3 – 10^6 . The electrons impinge on a scintillator screen, and the image is
648 recorded by a high-speed CCD camera for reconstruction of the transverse beam distribution.

649 An option for fast, turn-by-turn beam size diagnostics is an ionization profile monitor (IPM).

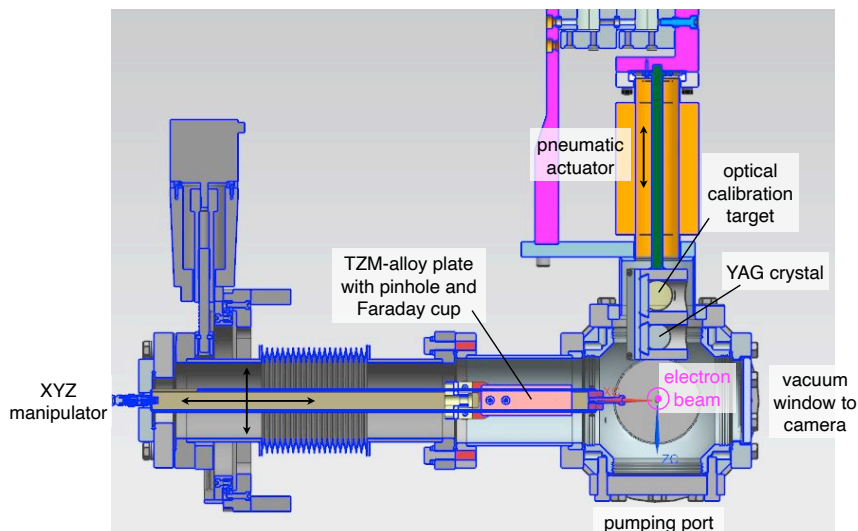


Figure 6. Layout of the diagnostic station.

650 This device collects ions from ionizations induced by the proton beam to generate a beam profile.
651 The amount of signal is proportional to the ionization cross section and the gas density. The gas
652 source can either be the residual gas or an injected gas. Horizontal and vertical IPMs have been
653 recently used for advanced studies in the Fermilab Booster proton synchrotron [114, 115]. In IOTA,
654 the residual gas pressure will be lower than it is in the Booster. However, the ionization cross section
655 for 2.5 MeV protons is two orders of magnitudes larger, yielding comparable signal rates. In IOTA,
656 IPMs similar to those in the Booster, i.e. without external guiding magnetic field, will have another
657 important advantage. According to an analysis presented in ref. [116], the expansion of the ions due
658 to the charge of the proton beams is minimal (of the order of 1%, compared to factors as large as 2
659 in the Booster), introducing negligible systematics in the turn-by-turn reconstruction of the proton
660 beam profiles.

661 Finally, operation of the IOTA electron lens as an electron cooler opens up an additional
662 diagnostic opportunity — the detection of neutral hydrogen from recombination, as described in
663 section 2.2. A recombination monitor will be installed behind the first dipole magnet downstream
664 of the electron lens (M4R in figure 1) to detect neutral hydrogen atoms H^0 formed in the electron
665 lens when the velocity of the magnetized beam matches that of the circulating protons. The rate
666 of neutralization events is used to tune the cooler settings. In addition, the transverse distribution
667 of H^0 provides a relatively fast (~ 1 s), minimally invasive estimate of the proton distribution. As
668 a detector, we are considering microchannel plates and a phosphor screen read out with a CCD
669 camera or a position-sensitive silicon detector.

670 The range of 2.5 MeV protons in metal is smaller than the beam pipe thickness. Proton
671 losses can only be directly monitored inside the vacuum chamber. Prototype in-vacuum diamond
672 detectors have been used in other machines [117, 118]. They are being considered for proton loss
673 measurements in IOTA as well.

674 The inclusion of an additional instrument for the IOTA electron lens is under study. A pickup
675 antenna could be installed in the vacuum chamber inside the main solenoid to sense cyclotron
676 radiation emitted by the magnetized electrons. Such a receiver can be used to monitor the electron
677 plasma density and temperature (besides providing a very accurate measurement of the magnetic
678 field) by recording the position, intensity and width of the cyclotron frequency peak (expected at
679 2.8 GHz in a 0.1 T field, for instance). The device was proposed for electron cooling [119–121] and
680 similar systems were applied to other precision measurements [122–124]. An operational system
681 would provide a new sensitive tool for electron lenses, especially for electron cooling and electron
682 columns.

683 **4.5 The Fermilab Electron-Lens Test Stand**

684 The Fermilab electron-lens test stand is a laboratory dedicated to the study of beam physics and
685 technology related to electron lenses. It was set up in the late 1990s in support of the first electron
686 lenses, built for the Tevatron collider [125, 126]. It has been used to characterize high-perveance
687 electron guns, to measure the effects of space charge on magnetized beam dynamics, and to study
688 trapped plasma columns. In recent years, it was instrumental in the development of hollow electron
689 lenses for beam halo control in the Tevatron [22] and in the LHC [29]. The IOTA research program
690 on nonlinear integrable optics relies on electron guns with specific current-density distributions.
691 Electron sources for cooling and space-charge compensation can also be tested here.

692 This test stand has been operational for over 20 years and it has been the only electron-lens
 693 test stand in the world for long periods of time. A similar facility was built at Brookhaven National
 694 Laboratory to support the RHIC electron-lens project [109], but it has since been decommissioned.
 695 A test stand for the HL-LHC hollow electron lenses is currently being developed at CERN.

696 The main experimental apparatus consists of a pulsed electron gun, a straight beam line with
 697 pickup electrodes, and a water-cooled collector (figure 7). The vacuum chamber is surrounded
 698 by three, independently powered resistive solenoids: the gun solenoid, the main solenoid, and the
 699 collector solenoid. The maximum magnetic field is 0.4 T. Magnetic correctors are used to steer the
 700 electron beam. End-plates in the metal shell of the solenoid are used to improve the uniformity of
 701 the axial magnetic field. The device is supported and aligned on a girder.

702 Current to the solenoids is provided by four 150 kW, 5 kA power converters. In steady state, at
 703 the maximum magnetic field, the solenoids dissipate about 210 kW through the low-conductivity
 704 water circuits. The vacuum system includes a diaphragm and turbomolecular pump for fore vacuum
 705 and ion-getter pumps to reach the operating pressures, which are typically 10^{-7} hPa to 10^{-8} hPa.
 706 The inner diameter of the beam pipe and of the pickup electrodes is 60 mm.

707 The cathode of the electron gun can be biased down to $V_c = -10$ kV. The anode is pulsed
 708 from V_c up to 0 V for beam extraction at a maximum rate of 10 kHz by a high-voltage modulator.

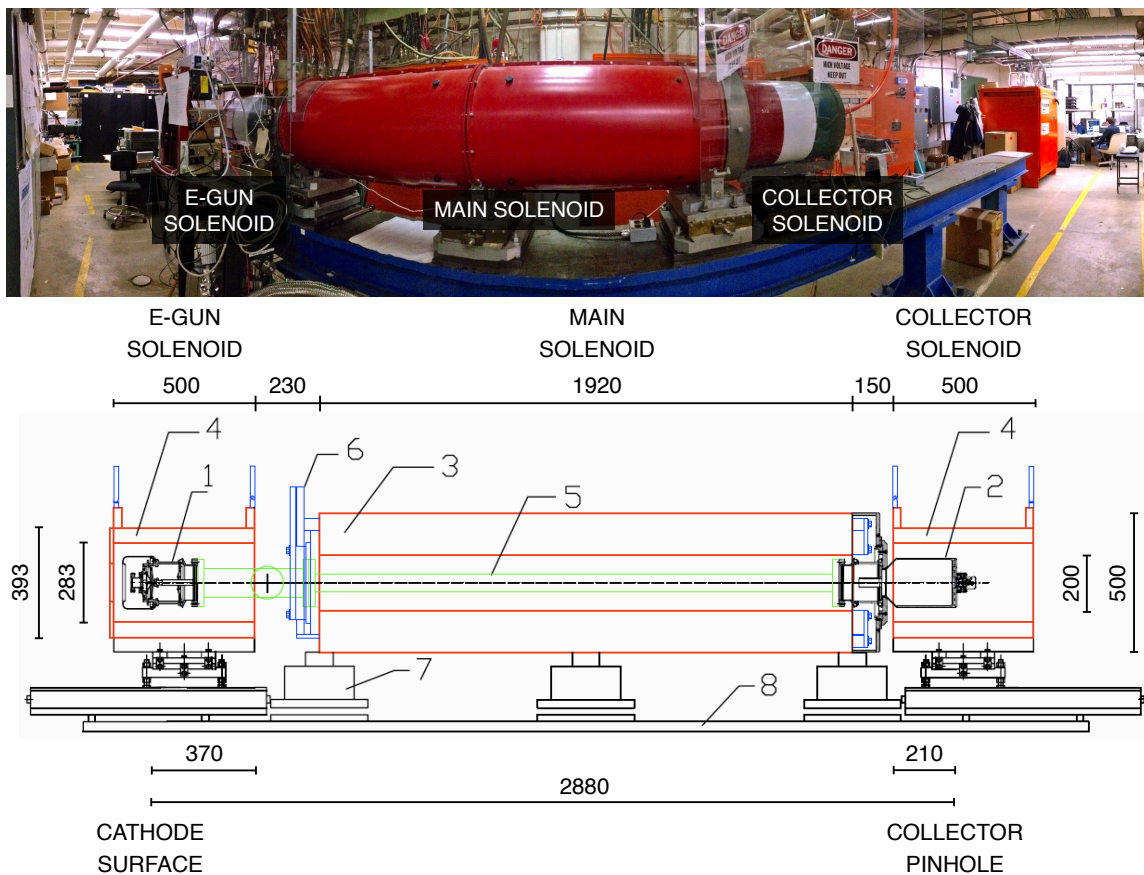


Figure 7. The Fermilab electron-lens test stand. Dimensions are in millimeters. (Photo: Valentina Previtali / Fermilab)

709 Typical pulse widths are between 200 ns and 20 μ s. The control system is integrated with the rest
710 of the Fermilab complex (ACNET). However, solenoid settings, high-voltage power supplies and
711 cathode filament heater are often controlled locally in manual mode.

712 Several types of electron guns have been designed and built to provide different intensities, beam
713 sizes, and current-density profiles (flat, Gaussian, hollow, etc.). The electron source is typically
714 based on a thermionic cathode. The electron-gun assemblies share the similar form factors and the
715 same flange adapters, so that they can be swapped easily.

716 The total beam current and pulse shape are measured with passive transformers at the cathode
717 and at the collector. The current-density profiles are measured by recording the average current
718 through a 0.2-mm-diameter pinhole in the collector, as a function of the settings of the horizontal
719 and vertical magnetic correctors. An example of current-density profile measurement is shown in
720 figure 5 above.

721 **5 Conclusions**

722 An exciting beam physics program is being carried out with the IOTA storage ring at Fermilab
723 and the first results have been published. The IOTA electron lens will be a key component of
724 upcoming studies on nonlinear integrable optics, space-charge compensation, electron cooling, and
725 the stability of intense beams in general. For the first time, several functions are being combined in
726 a compact device, yielding technical challenges but also new opportunities for research, training,
727 and collaboration.

728 **Acknowledgments**

729 We would like to thank the Beam Dynamics Panel of the International Committee for Future
730 Accelerators (ICFA) and its chair, prof. I. Hofmann, for curating this Special Issue on electron
731 lenses. Our Fermilab colleagues and the whole FAST/IOTA team made this research possible, in
732 particular D. Broemmelsiek, D. Edstrom, D. Franck, W. Johnson (retired), V. Kashikhin, J. Leibfritz,
733 M. McGee (retired), L. Nobrega, M. Obryki, J. Thangaraj, L. Valerio and T. Zolkin. We have greatly
734 benefited from the growing international community of electron-lens experts, including W. Fischer
735 and X. Gu of Brookhaven National Laboratory, A. Levichev and D. Nikiforov of the Budker
736 Institute of Nuclear Physics, and D. Mirarchi, S. Redaelli, A. Rossi, and S. Sadovich of CERN.
737 Prof. A. Pikkarainen of Kemi University of Applied Sciences (Finland) and students H. Schmuul and
738 J. Suopajarvi contributed to the mechanical designs. This work was supported in part by Phase I
739 Small Business Innovation Research (SBIR) Award No. DE-SC0020928 of the U.S. Department
740 of Energy. This manuscript has been authored by Fermi Research Alliance, LLC under Contract
741 No. DE-AC02-07CH11359 with the U.S. Department of Energy, Office of Science, Office of High
742 Energy Physics.

743 **References**

- 744 [1] S. Antipov, D. Broemmelsiek, D. Bruhwiler, D. Edstrom, E. Harms, V. Lebedev et al., *IOTA*
745 *(Integrable Optics Test Accelerator): Facility and experimental beam physics program*, *JINST* **12**
746 [\(2017\) T03002](#).

- 747 [2] A.G. Ruggiero, *Integrability of the two-dimensional beam-beam interaction in a special case, Part.*
748 *Accel.* **12** (1982) 45.
- 749 [3] V.V. Danilov and E.A. Perevedentsev, *On invariants and integrability in nonlinear accelerator*
750 *optics*, Tech. Rep. [SL-NOTE-94-74-AP](#), CERN, Geneva, Switzerland (1994).
- 751 [4] V.V. Danilov and E.A. Perevedentsev, *Two examples of integrable systems with round colliding*
752 *beams*, in *Proceedings of the IEEE Particle Accelerator Conference (PAC07)*, pp. 1759–1761, 1998,
753 [DOI](#).
- 754 [5] V. Danilov and S. Nagaitsev, *Nonlinear accelerator lattices with one and two analytic invariants*,
755 *Phys. Rev. ST Accel. Beams* **13** (2010) 084002.
- 756 [6] S.A. Antipov, S. Nagaitsev and A. Valishev, *Single-particle dynamics in a nonlinear accelerator*
757 *lattice: Attaining a large tune spread with octupoles in IOTA*, *JINST* **12** (2017) P04008.
- 758 [7] C.E. Mitchell, R.D. Ryne and K. Hwang, *Bifurcation analysis of nonlinear Hamiltonian dynamics in*
759 *the Fermilab Integrable Optics Test Accelerator*, *Phys. Rev. Accel. Beams* **23** (2020) 064002.
- 760 [8] A. Valishev, N. Kuklev, A. Romanov, G. Stancari and S. Szustkowski, *Nonlinear integrable optics*
761 *(NIO) in IOTA Run 2*, Tech. Rep. [Beams-doc-8871](#), Fermilab (2020).
- 762 [9] S. Szustkowski, *Nonlinear Integrable Optics Beam Dynamics Experiment and Diagnostics*, Ph.D.
763 thesis, Northern Illinois University, DeKalb, Illinois, USA, Dec., 2020.
- 764 [10] N. Kuklev, *Nonlinear integrable optics studies at IOTA*, Tech. Rep. [Beams-doc-8916](#), Fermilab
765 (Dec., 2020).
- 766 [11] M. Hofer, R. Tomás Garcia, A. Romanov, G. Stancari, A. Valishev, N. Kuklev et al., *Nonlinear*
767 *optics measurements in IOTA*, Tech. Rep. [FERMILAB-FN-1119-AD](#),
768 [CERN-ACC-NOTE-2021-0010](#), CERN (Mar., 2021).
- 769 [12] I. Lobach, V. Lebedev, S. Nagaitsev, A. Romanov, G. Stancari, A. Valishev et al., *Statistical*
770 *properties of spontaneous synchrotron radiation with arbitrary degree of coherence*, *Phys. Rev.*
771 *Accel. Beams* **23** (2020) 090703.
- 772 [13] I. Lobach, S. Nagaitsev, V. Lebedev, A. Romanov, G. Stancari, A. Valishev et al., *Transverse beam*
773 *emittance measurement by undulator radiation power noise*, *Phys. Rev. Lett.* **126** (2021) 134802.
- 774 [14] I. Lobach, S. Nagaitsev, V. Lebedev, A. Romanov, G. Stancari, A. Valishev et al., *Measurements of*
775 *undulator radiation power noise and comparison with Ab Initio calculations*, *Phys. Rev. Accel.*
776 *Beams* **24** (2021) 040701.
- 777 [15] V. Lebedev, J. Jarvis, H. Piekarz, A. Romanov, J. Ruan and M. Andorf, *Conceptual design report:*
778 *Optical stochastic cooling at IOTA*, Tech. Rep. [FERMILAB-PUB-20-656-AD](#), Fermilab (Dec.,
779 2020).
- 780 [16] G. Stancari, “Detecting single electrons in IOTA.” talk presented at the Workshop on
781 Single-Electron Experiments in IOTA, Fermilab,
782 <https://indico.fnal.gov/event/18395/contributions/46977>, Nov., 2018.
- 783 [17] A. Romanov, J. Santucci, G. Stancari, A. Valishev and N. Kuklev, *Experimental 3-dimensional*
784 *tracking of the dynamics of a single electron in the Fermilab Integrable Optics Test Accelerator*
785 *(IOTA)*, submitted to *Phys. Rev. Accel. Beams* (2020) [[2012.04148](#)].
- 786 [18] “IOTA/FAST Scientific Committee (ISC) Web page.”
787 <https://cdcvs.fnal.gov/redmine/projects/ifsc/wiki>.

- 788 [19] V. Shiltsev, Y. Alexahin, K. Bishofberger, V. Kamerdzhev, G. Kuznetsov and X.-L. Zhang,
789 *Experimental demonstration of colliding-beam-lifetime improvement by electron lenses*, *Phys. Rev.*
790 *Lett.* **99** (2007) 244801.
- 791 [20] V. Shiltsev, K. Bishofberger, V. Kamerdzhev, S. Kozub, M. Kufer, G. Kuznetsov et al., *Tevatron*
792 *electron lenses: Design and operation*, *Phys. Rev. ST Accel. Beams* **11** (2008) 103501.
- 793 [21] X.-L. Zhang, K. Bishofberger, V. Kamerdzhev, V. Lebedev, V. Shiltsev, R. Thurman-Keup et al.,
794 *Generation and diagnostics of uncaptured beam in the Fermilab Tevatron and its control by electron*
795 *lenses*, *Phys. Rev. ST Accel. Beams* **11** (2008) 051002.
- 796 [22] G. Stancari, A. Valishev, G. Annala, G. Kuznetsov, V. Shiltsev, D.A. Still et al., *Collimation with*
797 *hollow electron beams*, *Phys. Rev. Lett.* **107** (2011) 084802.
- 798 [23] W. Fischer, X. Gu, Z. Altinbas, M. Costanzo, J. Hock, C. Liu et al., *Operational head-on beam-beam*
799 *compensation with electron lenses in the Relativistic Heavy Ion Collider*, *Phys. Rev. Lett.* **115** (2015)
800 264801.
- 801 [24] I. Béjar Alonso, O. Brüning, P. Fessia, M. Lamont, L. Rossi, L. Taviani et al., eds., *High-Luminosity*
802 *Large Hadron Collider (HL-LHC): Technical Design Report*, CERN Yellow Reports: Monographs,
803 CERN, Geneva, Switzerland (2020), [10.23731/CYRM-2020-0010](https://arxiv.org/abs/10.23731/CYRM-2020-0010).
- 804 [25] G. Stancari, V. Previtali, A. Valishev, R. Bruce, S. Redaelli, A. Rossi et al., *Conceptual design of*
805 *hollow electron lenses for beam halo control in the Large Hadron Collider*, Tech. Rep.
806 [FERMILAB-TM-2572-APC](https://arxiv.org/abs/10.23731/CYRM-2020-0010), Fermilab (May, 2014).
- 807 [26] D. Perini, G. Gobbi, D.J. Crawford, J. Ruan, G. Stancari, L.R. Valerio et al., *The development*
808 *programme of cathodes and electron guns for the hollow electron lenses of the High Luminosity*
809 *LHC Project*, in *Proceedings of the 10th International Particle Accelerator Conference (IPAC19)*,
810 no. FERMILAB-CONF-19-337-AD, (Melbourne, Australia), JACoW, May, 2019, [DOI](https://arxiv.org/abs/10.23731/CYRM-2020-0010).
- 811 [27] X. Gu, W. Fischer, Z. Altinbas, A. Drees, J. Hock, R. Hulsart et al., *Halo removal experiments with*
812 *hollow electron lens in the BNL Relativistic Heavy Ion Collider*, *Phys. Rev. Accel. Beams* **23** (2020)
813 031001.
- 814 [28] M. Fitterer, G. Stancari, A. Valishev, S. Redaelli and D. Valuch, *Resonant and random excitations on*
815 *the proton beam in the Large Hadron Collider for active halo control with pulsed hollow electron*
816 *lenses*, *Phys. Rev. Accel. Beams* **24** (2021) 021001.
- 817 [29] S. Redaelli, R.B. Appleby, R. Bruce, O. Brüning, A. Kolehmainen, G. Ferlin et al., *Hollow electron*
818 *lenses for beam collimation at the High-Luminosity Large Hadron Collider (HL-LHC)*, *JINST* **16**
819 (2021) P03042.
- 820 [30] D. Mirarchi, R.B. Appleby, R. Bruce, G. Giovannozzi, A. Mereghetti, S. Redaelli et al., *Nonlinear*
821 *dynamics of proton beams with hollow electron lens in the CERN High-Luminosity LHC*, submitted
822 to *European Physical Journal Plus* (2021) .
- 823 [31] S. Artikova, O. Boine-Frankenheim, O. Meusel, A. Oeftiger, D. Ondreka, K. Schulte-Urlichs et al.,
824 *Pulsed electron lenses for space charge compensation in the FAIR synchrotrons*, *JINST* **16** (2021)
825 P03044.
- 826 [32] V.D. Shiltsev, *Electron Lenses for Super-Colliders*, Springer (2016), [10.1007/978-1-4939-3317-4](https://arxiv.org/abs/10.1007/978-1-4939-3317-4).
- 827 [33] V.V. Danilov and V.D. Shiltsev, “Round colliding beams” as a way to integrability: Theory and
828 simulations for Tevatron, Tech. Rep. [FERMILAB-FN-655](https://arxiv.org/abs/10.23731/CYRM-2020-0010), Fermilab (Feb., 1997).
- 829 [34] V.V. Danilov and V.D. Shiltsev, *On possibility of footprint compression with one lens in nonlinear*
830 *accelerator lattice*, Tech. Rep. [FERMILAB-FN-671](https://arxiv.org/abs/10.23731/CYRM-2020-0010), Fermilab (July, 1998).

- 831 [35] V. Danilov and V. Shiltsev, *On the possibility of footprint compression with one lens in nonlinear*
832 *accelerator lattice*, *JINST* **16** (2021) P03050.
- 833 [36] S. Nagaitsev and T. Zolkin, *Betatron frequency and the Poincaré rotation number*, *Phys. Rev. Accel.*
834 *Beams* **23** (2020) .
- 835 [37] E.M. McMillan, *Some thoughts on stability in nonlinear periodic focusing systems*, Tech. Rep.
836 [UCRL-17795](#), Lawrence Radiation Laboratory, University of California, Berkeley, California (Sept.,
837 1967).
- 838 [38] E.M. McMillan, *A problem in the stability of periodic systems*, in *Topics in Modern Physics: A*
839 *Tribute to Edward U. Condon*, W.E. Brittin and H. Odabasi, eds., (Boulder, Colorado), pp. 219–244,
840 Colorado Associated University Press (1971).
- 841 [39] B. Cathey, G. Stancari, A. Valishev and T. Zolkin, *Calculations of detuning with amplitude for the*
842 *McMillan electron lens in the Fermilab Integrable Optics Test Accelerator (IOTA)*, *JINST* **16** (2021)
843 [P03041](#).
- 844 [40] G. Stancari, A. Burov, V. Lebedev, S. Nagaitsev, E. Prebys and A. Valishev, *Electron lenses and*
845 *cooling for the Fermilab Integrable Optics Test Accelerator*, in *Proceedings of the International*
846 *Workshop on Beam Cooling and Related Topics (COOL2015)*, (Newport News, Virginia, USA),
847 p. 32, JACoW, Nov., 2015, DOI [[1511.01812](#)].
- 848 [41] H. Poth, *Electron cooling: Theory, experiment, application*, *Phys. Rep.* **196** (1990) 135.
- 849 [42] G. Tranquille et al., *Commissioning the ELENA beam diagnostics systems at CERN*, in *Proceedings*
850 *of the 9th International Particle Accelerator Conference (IPAC2018)*, pp. 2043–2046, JACoW
851 Publishing, June, 2018, DOI.
- 852 [43] L.D. Landau, *On the vibrations of the electronic plasma*, *J. Phys. (USSR)* **10** (1946) 25.
- 853 [44] J.S. Berg and F. Ruggiero, *Landau damping with two-dimensional betatron tune spread*, Tech. Rep.
854 [CERN-SL-96-071-AP](#), CERN, Geneva (Dec., 1996).
- 855 [45] A. Burov, *Nested head-tail Vlasov solver*, *Phys. Rev. ST Accel. Beams* **17** (2014) 021007.
- 856 [46] R. Tomás, M. Benedikt, A.V. Bogomyagkov, L. Bottura, F. Cerutti, L.S. Esposito et al., *FCC study:*
857 *Parameters and optics for hadron and lepton colliders*, *Nucl. Part. Phys. Proc.* **273–275** (2016) 149.
- 858 [47] M. Benedikt and F. Zimmermann, *Towards future circular colliders*, *J. Korean Phys. Soc.* **69** (2016)
859 893.
- 860 [48] D. Schulte, “FCC-hh layout and parameters.” talk presented at the [3rd Annual Meeting of the Future](#)
861 [Collider Study](#), Berlin, Germany,
862 <https://indico.cern.ch/event/556692/contributions/2484245/>, May, 2017.
- 863 [49] W. Scandale, *Dynamic aperture*, *AIP Conf. Proc.* **326** (1995) 52.
- 864 [50] V. Shiltsev, Y. Alexahin, A. Burov and A. Valishev, *Landau damping of beam instabilities by*
865 *electron lenses*, *Phys. Rev. Lett.* **119** (2017) 134802.
- 866 [51] O. Boine-Frankenheim and W.D. Stem, *Space charge compensation with pulsed electron lenses for*
867 *intense ion beams in synchrotrons*, *Nucl. Instrum. Methods Phys. Res. A* **896** (2018) 122.
- 868 [52] R. Ainsworth, “Ensuring bunch stability in multi-MW beams.” Department of Energy Early Career
869 Research Program for Fiscal Year 2020, [URL](#), 2020.
- 870 [53] A. Burov, G.W. Foster and V.E. Shiltsev, *Space-charge compensation in high-intensity proton rings*,
871 Tech. Rep. [FNAL-TM-2125](#), Fermilab (Sept., 2000).

- 872 [54] Y. Alexahin, A. Drozhdin, N. Kazarinov and X. Yang, *Effects of space charge and magnet*
873 *nonlinearities on beam dynamics in the Fermilab Booster*, in *Proceedings of the 22nd Particle*
874 *Accelerator Conference (PAC07)*, (Albuquerque, New Mexico, USA), pp. 3474–3476, 2007, DOI.
- 875 [55] Y. Alexahin and V. Kapin, *Study of possibility of space charge compensation in the Fermilab*
876 *Booster with multiple electron columns*, Tech. Rep. [Beams-doc-3108](#), Fermilab (June, 2008).
- 877 [56] Y. Alexahin and V. Kapin, *On possibility of space-charge compensation in the Fermilab Booster*
878 *with multiple electron columns*, *JINST* **16** (2021) P03049.
- 879 [57] V.N. Litvinenko and G. Wang, *Compensating tune spread induced by space charge in bunched*
880 *beams*, *Phys. Rev. ST Accel. Beams* **17** (2014) 114401.
- 881 [58] D. Ondreka, P. Spiller, P. Apse-Apsitis and K. Schulte, *Overcoming the space charge limit:*
882 *Development of an electron lens for SIS18*, in *Proceedings of the 8th International Particle*
883 *Accelerator Conference (IPAC2017)*, pp. 2211–2213, 2017, DOI.
- 884 [59] E. Stern, *PIC simulations of space charge compensation with electron lens*, Tech. Rep.
885 [Beams-doc-7567](#), Fermilab (Aug., 2019).
- 886 [60] E. Stern, Y. Alexahin, A. Burov and V. Shiltsev, *Self-consistent PIC simulations of ultimate space*
887 *charge compensation with electron lenses*, *JINST* **16** (2021) P03045.
- 888 [61] J.S. DeGrassie and J.H. Malmberg, *Wave-induced transport in the pure electron plasma*, *Phys. Rev.*
889 *Lett.* **39** (1977) 1077.
- 890 [62] D.H.E. Dubin and T.M. O’Neil, *Trapped nonneutral plasmas, liquids, and crystals (the thermal*
891 *equilibrium states)*, *Rev. Mod. Phys.* **71** (1999) 87.
- 892 [63] V.D. Shiltsev, *On possibility to compensate space charge effects by controlled electron columns*,
893 Tech. Rep. [FNAL-Beams-doc-2810-v1](#), Fermilab (June, 2007).
- 894 [64] V.D. Shiltsev, *New possibilities for beam-beam and space-charge compensation: MCP gun and*
895 *electron columns*, in *Proceedings of the 22nd Particle Accelerator Conference (PAC07)*,
896 (Albuquerque, NM, USA), pp. 1159–1160, June, 2007,
897 <https://accelconf.web.cern.ch/p07/PAPERS/TUPMN106.PDF>.
- 898 [65] G.I. Budker, G.I. Dimov, V.G. Dudnikov, A.A. Sokolov and V.G. Shamovsky, *Experiments on*
899 *electron compensation of proton beam in ring accelerator*, in *Proceedings of the 6th International*
900 *Conference on High-Energy Accelerators (HEACC67)*, pp. A103–A105, 1967,
901 <https://inspirehep.net/literature/921150>.
- 902 [66] Y.I. Belchenko, G.I. Budker, G.E. Derevyankin, G.I. Dimov, V.G. Dunikov, G.V. Roslyakov et al.,
903 *High current proton beams at Novosibirsk*, in *Proceedings of the 10th International Conference on*
904 *High-Energy Accelerators (HEACC77)*, pp. 287–294, 1977, <https://inspirehep.net/literature/127164>.
- 905 [67] Y.I. Belchenko, *High current proton beams at Novosibirsk: Electron compensation, charge exchange*
906 *injection, negative ion sources*, Tech. Rep. [LA-TR-78-53](#), [CONF-770709-23](#), Fermilab (1978).
- 907 [68] G.I. Dimov and V.E. Chupriyanov, *Compensated proton-beam production in an accelerating ring at*
908 *a current above the space-charge limit*, *Part. Accel.* **14** (1984) 155.
- 909 [69] V. Dudnikov, *Condition for production of circulating proton beam with intensity greater than space*
910 *charge limit*, *AIP Conf. Proc.* **642** (2002) 367.
- 911 [70] V.D. Shiltsev, A. Valishev, G. Kuznetsov, V. Kamerzhiev and A. Romanov, *Beam studies with*
912 *electron columns*, in *Proceedings of the 23rd Particle Accelerator Conference (PAC09)*, (Vancouver,

- 913 BC, Canada), pp. 3233–3235, IEEE, May, 2009,
914 <https://accelconf.web.cern.ch/pac2009/papers/th5fp020.pdf>.
- 915 [71] R.E. Pollock, J. Ellsworth, M.W. Muterspaugh and D.S. Todd, *Proton beam – electron plasma*
916 *interactions*, *AIP Conf. Proc.* **498** (1999) 336.
- 917 [72] D.S. Todd and R.E. Pollock, *An experiment to transfer angular momentum from a helical low energy*
918 *proton beam to a trapped electron plasma*, *AIP Conf. Proc.* **606** (2002) 223.
- 919 [73] M.E. Rudd, Y.-K. Kim, D.H. Madison and J.W. Gallagher, *Electron production in proton collisions:*
920 *Total cross sections*, *Rev. Mod. Phys.* **57** (1985) 965.
- 921 [74] M. Chung, L. Prost and V.D. Shiltsev, *Space-charge compensation for high-intensity linear and*
922 *circular accelerators at fermilab*, in *Proceedings of the 2013 North American Particle Accelerator*
923 *Conference (PAC2013)*, (Pasadena, CA, USA), pp. 402–404, Sept., 2013,
924 <https://accelconf.web.cern.ch/pac2013/papers/tuobb1.pdf>.
- 925 [75] C.S. Park, V.D. Shiltsev, G. Stancari, J.C.T. Thangaraj and D. Milana, *Space charge compensation*
926 *using electron columns and electron lenses at IOTA*, in *Proceedings of the 2016 North American*
927 *Particle Accelerator Conference (NAPAC2016)*, (Chicago, IL, USA), pp. 1257–1259, JACoW, Oct.,
928 2016, DOI.
- 929 [76] B.T. Freemire, S. Chattopadhyay, V.D. Shiltsev, G. Stancari, C.S. Park, G. Penn et al., *Simulations of*
930 *the electron column in IOTA*, in *Proceedings of the 9th International Particle Accelerator Conference*
931 *(IPAC2018)*, (Vancouver, BC, Canada), pp. 1103–1106, JACoW Publishing, Apr., 2018, DOI.
- 932 [77] B.T. Freemire, S. Chattopadhyay, V.D. Shiltsev, G. Stancari, C.S. Park, G. Penn et al., *Space-charge*
933 *compensation using electron columns at IOTA*, in *Proceedings of the 61st Advanced Beam*
934 *Dynamics Workshop on High-Intensity and High-Brightness Hadron Beams (HB2018)*, (Daejeon,
935 South Korea), pp. 247–251, JACoW Publishing, June, 2018, DOI.
- 936 [78] B.T. Freemire, S. Chattopadhyay, E.G. Stern, C.S. Park, C.E. Mitchell, R.D. Ryne et al., *Multipass*
937 *simulations of space charge compensation using an electron column at IOTA*, in *Proceedings of the*
938 *10th International Particle Accelerator Conference (IPAC2019)*, (Melbourne, Australia),
939 pp. 3313–3316, JACoW Publishing, May, 2019, DOI.
- 940 [79] A. Friedman et al., *Computational methods in the Warp code framework for kinetic simulations of*
941 *particle beams and plasmas*, *IEEE Trans. Plasma Sci.* **42** (2014) 1321.
- 942 [80] “Warp.” <http://warp.lbl.gov>.
- 943 [81] J. Amundson, P. Spentzouris, J. Qiang and R. Ryne, *Synergia: An accelerator modeling tool with*
944 *3-D space charge*, *J. Comp. Phys.* **211** (2006) 229.
- 945 [82] “Synergia.” <https://synergia.fnal.gov>.
- 946 [83] C.S. Park, B. Freemire, M. Chung, G. Stancari and E. Stern, *Progress in space charge compensation*
947 *using electron columns*, *JINST* **16** (2021) P03048.
- 948 [84] A. Kalimov, C. Muehle, D. Ondreka, K. Schulte-Urlichs and P. Spiller, *Optimization of a solenoid*
949 *for an electron lens in SIS18*, *IEEE Trans. Appl. Supercond.* **30** (2020) 1.
- 950 [85] Y. Alexahin, A. Burov and V. Shiltsev, *Landau damping with electron lenses in space-charge*
951 *dominated beams*, Tech. Rep. FERMILAB-TM-2655-APC, Fermilab (2017).
- 952 [86] Y. Alexahin, A. Burov and V. Shiltsev, *Landau damping with electron lenses in space-charge*
953 *dominated beams*, *JINST* **16** (2021) P03046.

- 954 [87] A. Burov, V. Danilov and V. Shiltsev, *Transverse beam stability with an “electron lens”*, *Phys. Rev.*
955 *E* **59** (1999) 3605.
- 956 [88] I. Lobach, S. Nagaitsev, E. Stern and T. Zolkin, *McMillan lens in a system with space charge*, in
957 *Proceedings of the 9th International Particle Accelerator Conference (IPAC2018)*, (Vancouver,
958 Canada), p. 3143, Apr., 2018, DOI.
- 959 [89] S. Nagaitsev, I. Lobach, E. Stern and T. Zolkin, *McMillan electron lens in a system with space*
960 *charge*, *JINST* **16** (2021) P03047.
- 961 [90] R.C. Dhuley, C. Boffo, V. Kashikhin, A. Kolehmainen, D. Perini and G. Stancari, *Design of a*
962 *compact, cryogen-free superconducting solenoid for the electron lens of the Fermilab Integrable*
963 *Optics Test Accelerator (IOTA)*, *JINST* **16** (2021) T03009.
- 964 [91] D.A. Edwards and L.C. Teng, *Parametrization of linear coupled motion in periodic systems*, *IEEE*
965 *Trans. Nucl. Sci.* **20** (1973) 885.
- 966 [92] F. Willeke and G. Ripken, *Methods of beam optics*, *AIP Conf. Proc.* **184** (1989) 758.
- 967 [93] V.A. Lebedev and S.A. Bogacz, *Betatron motion with coupling of horizontal and vertical degrees of*
968 *freedom*, *JINST* **5** (2010) P10010.
- 969 [94] L. Deniau, H. Grote, G. Roy and F. Schmidt, “MAD – Methodical Accelerator Design.”
970 <http://mad.web.cern.ch/mad>.
- 971 [95] A. Burov, *Electron drift instability in storage rings with electron cooling*, *Nucl. Instrum. Methods*
972 *Phys. Res. A* **441** (2000) 23.
- 973 [96] A. Burov, *Two-beam instability in electron cooling*, *Phys. Rev. ST Accel. Beams* **9** (2006) 120101.
- 974 [97] Y.H. Jo, J.S. Kim, G. Stancari, M. Chung and H.J. Lee, *Control of the diocotron instability of a*
975 *hollow electron beam with periodic dipole magnets*, *Phys. Plasmas* **25** (2018) 011607.
- 976 [98] G. Stancari, “Electron-beam simulations: Electron-gun emission and residual fields from measured
977 profiles.” talk presented at the CERN Meeting on Hollow Electron Lens Beam Results,
978 <https://indico.cern.ch/event/698949/contributions/2868279>, Jan., 2018.
- 979 [99] R.C. Davidson, *Physics of Nonneutral Plasmas*, World Scientific (2001).
- 980 [100] D. Noll and G. Stancari, *Field calculations, single-particle tracking, and beam dynamics with space*
981 *charge in the electron lens for the Fermilab Integrable Optics Test Accelerator*, Tech. Rep.
982 [FERMILAB-TM-2598-AD-APC](https://arxiv.org/abs/1508.01001), Fermilab (2015), DOI.
- 983 [101] D. Noll, M. Droba, O. Meusel, U. Ratzinger, K. Schulte and C. Wiesner, *The particle-in-cell code*
984 *bender and its application to non-relativistic beam transport*, in *Proceedings of the 54th ICFA*
985 *Advanced Beam Dynamics Workshop on High Intensity, High Brightness and High Power Hadron*
986 *Beams (HB2014)*, pp. 304–308, 2015, <http://accelconf.web.cern.ch/HB2014/papers/weo4lr02.pdf>.
- 987 [102] “COMSOL Multiphysics.” <https://www.comsol.com>.
- 988 [103] “CST Studio Suite.” Dessault Systèmes, <https://www.3ds.com>.
- 989 [104] R. Dhuley, *Cooldown analysis of the IOTA electron-lens superconducting magnet with cryocooler*
990 *conduction cooling*, Tech. Rep. FERMILAB-TM-2738-AD-TD, Fermilab (Apr., 2020).
- 991 [105] D. Perini, A. Kolehmainen, A. Rossi, S. Sadovich and G. Stancari, *Design of high-performance guns*
992 *for the HL-LHC HEL*, *JINST* **16** (2021) T03010.
- 993 [106] A.N. Sharapa and A.V. Shemyakin, *Electron cooling device without bending magnets*, *Nucl.*
994 *Instrum. Methods Phys. Res. A* **336** (1993) 6.

- 995 [107] V.M. Barbashin, S.N. Chumakov, G. Ciullo, N.S. Dikansky, G. Lamanna, P. Lenisa et al., *Prototype*
996 *of an electron cooling device without bending magnets*, *Nucl. Instrum. Methods Phys. Res. A* **366**
997 (1995) 215.
- 998 [108] G. Ciullo, A.N. Sharapa, A.V. Shemyakin and L. Tecchio, *Characteristics of the beams generated by*
999 *a ‘hollow cathode’ electron gun*, *Rev. Sci. Instrum.* **69** (1998) 59.
- 1000 [109] X. Gu, F.Z. Altinbas, E. Beebe, W. Fischer, B.M. Frak, D.M. Gassner et al., *The electron lens test*
1001 *bench for the Relativistic Heavy Ion Collider at Brookhaven National Laboratory*, *Nucl. Instrum.*
1002 *Methods Phys. Res. A* **743** (2014) 56.
- 1003 [110] X. Gu, Z. Altinbas, M. Costanzo, W. Fischer, D.M. Gassner, J. Hock et al., *Transverse profile of the*
1004 *electron beam for the RHIC electron lenses*, *Nucl. Instrum. Methods Phys. Res. A* **798** (2015) 36.
- 1005 [111] R.E. Pollock and F. Anderegg, *Spin-up of an electron plasma — first results*, *AIP Conf. Proc.* **331**
1006 (1995) 139.
- 1007 [112] E.M. Hollmann, F. Anderegg and C.F. Driscoll, *Confinement and manipulation of non-neutral*
1008 *plasmas using rotating wall electric fields*, *Phys. Plasmas* **7** (2000) 2776.
- 1009 [113] S. Szustkowski, S. Chattopadhyay, D.J. Crawford and B.T. Freemire, *Skimmer-nozzle configuration*
1010 *measurements for a gas sheet beam profile monitor*, in *Proceedings of the North American Particle*
1011 *Accelerator Conference (NAPAC19)*, (Lansing, Michigan, USA), p. 573, Sept., 2019, DOI.
- 1012 [114] J. Eldred, V. Lebedev, K. Seiya and V. Shiltsev, *Studies of beam intensity effects in Fermilab Booster*
1013 *synchrotron*, Tech. Rep. FERMILAB-PUB-20-673-AD-APC, Fermilab (Dec., 2020).
- 1014 [115] J. Eldred, V. Lebedev, K. Seiya and V. Shiltsev, *Beam intensity effects in Fermilab Booster*
1015 *synchrotron*, *Phys. Rev. Accel. Beams* **24** (2021) 044001.
- 1016 [116] V. Shiltsev, *Space-charge effects in ionization beam profile monitors*, *Nucl. Instrum. Methods Phys.*
1017 *Res. A* **986** (2021) 164744.
- 1018 [117] C. Xu, B. Dehning, F.S. Domingues Sousa and E. Griesmayer, *Diamond monitor based beam loss*
1019 *measurements in the LHC*, in *Proceedings of the 5th International Beam Instrumentation*
1020 *Conference (IBIC2016)*, (Barcelona, Spain), pp. 82–85, JACoW, 2016, DOI.
- 1021 [118] A.A. Warner, “Thin sCVD diamond halo/loss monitor.” Fermilab Lab Directed Research and
1022 Development (LDRD) Proposal (unpublished), 2015.
- 1023 [119] C. Rubbia, *Microwave radiation from the transverse temperature of an intense electron beam*
1024 *confined by a longitudinal magnetic field*, Tech. Rep. CERN-EP-77-4, CERN, Geneva, Switzerland
1025 (1977).
- 1026 [120] J. Bridges, J. Gannon, E.R. Gray, J. Griffin, F.R. Huson, D.E. Johnson et al., *Fermilab electron*
1027 *cooling experiment: Design report*, Tech. Rep. FERMILAB-DESIGN-1978-01, Fermilab, Batavia
1028 IL, USA (Aug., 1978), DOI.
- 1029 [121] G. Tranquille, *Diagnostics for electron cooled beams*, in *Proceedings of the European Workshop on*
1030 *Beam Diagnostics and Instrumentation for Particle Accelerators (DIPAC2003)*, A. Peters and
1031 V.R.W. Schaa, eds., no. CERN-AB-2003-059-BDI, (Mainz, Germany), p. 110, May, 2003,
1032 <http://accelconf.web.cern.ch/AccelConf/d03/papers/PM09.pdf>.
- 1033 [122] R.W. Gould and M.A. LaPointe, *Cyclotron resonance in a pure electron plasma column*, *Phys. Rev.*
1034 *Lett.* **67** (1991) 3685.
- 1035 [123] N.C. Luhmann, H. Bindslev, H. Park, J. Sánchez, G. Taylor and C.X. Yu, *Chapter 3: Microwave*
1036 *diagnostics*, *Fusion Sci. Technol.* **53** (2008) 335.

- 1037 [124] D.M. Asner, R.F. Bradley, L. de Viveiros, P.J. Doe, J.L. Fernandes, M. Fertl et al., *Single-electron*
1038 *detection and spectroscopy via relativistic cyclotron radiation*, *Phys. Rev. Lett.* **114** (2015) 162501.
- 1039 [125] C. Crawford, F. Niell, G. Saewert, J. Santucci, A. Sery, A. Shemyakin et al., *Prototype “electron*
1040 *lens” set-up for the Tevatron beam-beam compensation*, in *Proceedings of the 1999 Particle*
1041 *Accelerator Conference (PAC99)*, vol. 1, pp. 237–239, IEEE, 1999, DOI.
- 1042 [126] C. Crawford, A. Sery, V. Shiltsev, A. Aleksandrov, B. Skarbo and B. Sukhina, *Magnetic field*
1043 *alignment in the beam-beam compensation device*, in *Proceedings of the 1999 Particle Accelerator*
1044 *Conference*, vol. 5, pp. 3321–3323, IEEE, 1999, DOI.